The Astrophysical Journal, 864:90 (34pp), 2018 September 1 https://doi.org/10.3847/1538-4357/aad5ed

The Shocking Power Sources of LINERs*

Mallory Molina[1,8], Michael Eracleous[1], Aaron J. Barth[2], Dan Maoz[3], Jessie C. Runnoe[1,4], Luis C. Ho[5], Joseph C. Shields[6], and Jonelle L. Walsh[7]
[1] Department of Astronomy and Astrophysics and Institute for Gravitation and the Cosmos, The Pennsylvania State University, 525 Davey Lab, University Park, PA 16803, USA
[2] Department of Physics and Astronomy, 4129 Frederick Reines Hall, University of California, Irvine, CA, 92697-4575, USA
[3] School of Physics and Astronomy, Tel-Aviv University, Tel-Aviv 69978, Israel
[4] Department of Astronomy, University of Michigan, 1085 S. University Avenue, Ann Arbor, MI 48109, USA
[5] Kavli Institute for Astronomy and Astrophysics, Peking University, 5 Yiheyuan Road, Haidian District, Beijing 100871, People's Republic of China
[6] Department of Physics and Astronomy, Ohio University, Clippinger Labs 251, Athens, OH 45701, USA
[7] Mitchell Institute for Fundamental Physics and Astronomy, Department of Physics and Astronomy, Texas A&M University, 4242 TAMU, College Station, TX 77845, USA
Received 2018 April 17; revised 2018 July 16; accepted 2018 July 23; published 2018 September 4

Abstract

The majority of low-ionization nuclear emission-line regions (LINERs) harbor supermassive black holes with very low accretion rates. However, the accretion flows do not produce enough ionizing photons to power the emission lines emitted on scales of ∼100 pc, and therefore additional sources of power are required. We present and analyze *Hubble Space Telescope* spectra of three nearby luminous LINERs that are spatially resolved on scales of $\lesssim$9 pc. The targets have multiple indicators of an accreting black hole, as well as a deficient ionizing photon budget. We measure diagnostic emission line ratios as a function of distance from the nucleus and compare them to models for different excitation mechanisms: shocks, photoionization by the accreting black hole, and photoionization by young or old hot stars. We also consider the kinematics of the line-emitting gas, as revealed by the widths and shifts of the emission lines. We conclude that, in LINERs with low-luminosity active nuclei, shocks by jets or other outflows are crucial in exciting the gas in and around the nucleus, as suggested by other authors. The physical model that best describes our targets comprises a low-luminosity, accretion-powered active nucleus that photoionizes the gas within ∼20 pc of the galaxy center, and shock excitation of the gas at larger distances.

Key words: galaxies: active – galaxies: individual (NGC 1052), (NGC 4278), (NGC 4579) – galaxies: nuclei

1. Introduction

Low-ionization nuclear emission-line regions (LINERs) were first identified by Heckman (1980) based on the relative strengths of their low ionization lines and classified according to the ratios of their oxygen lines ([O II]λ3727/[O III]λ5007 $>$ 1 and [O I] λ6300/[O III]λ5007 $>$ 1/3). They are now known to be very common; they are found in approximately 50% of nearby galaxies (Ho et al. 1997b). A detailed discussion on the properties of LINERs is given in Ho (2008). The power source behind their emission lines has been under debate since their discovery and the following explanations have been considered with varying degrees of success in accurately describing their observational signatures: (1) photoionization by low-luminosity active galactic nuclei (LLAGNs) (Ferland & Netzer 1983; Halpern & Steiner 1983), (2) photoionization by young, hot stars such as Wolf-Rayet stars (Terlevich & Melnick 1985), hot O stars (Filippenko & Terlevich 1992; Shields 1992) and compact starbursts (Barth & Shields 2000), (3) photoionization by exposed cores of evolved stars such as post-asymptotic giant branch (pAGB) stars (Binette et al. 1994; Yan & Blanton 2012; Papaderos et al. 2013; Singh et al. 2013; Belfiore et al. 2016) and planetary nebulae (Taniguchi et al. 2000), and (4) collisional or photo-excitation either by slow, or fast, photoionizing shocks (Fosbury et al. 1978; Heckman 1980; Dopita et al. 1996, 1997). Models invoking a combination of the above power sources have also been considered (e.g., Contini 1997; Contini & Viegas 2001; Sabra et al. 2003; Martins et al. 2004).

The LLAGN interpretation of LINERs was initially motivated by their significant X-ray emission (Ferland & Netzer 1983; Halpern & Steiner 1983). Although LLAGNs are found via radio and X-ray observations in the majority of LINERs (Dudik et al. 2005, 2009; Nagar et al. 2005; Filho et al. 2006; Flohic et al. 2006; González-Martín et al. 2009), they are not powerful enough to photoionize the gas in their vicinity on ∼100 pc (i.e., a few arcseconds in nearby galaxies) scales on which the characteristic emission lines are detected (Flohic et al. 2006; Eracleous et al. 2010a, and references therein). Imaging studies of LINERs have found extended line-emitting regions and complex circumnuclear dust morphologies that might obscure and further prevent the LLAGNs from fully ionizing the surrounding gas (Barth et al. 1999; Pogge et al. 2000; Simões Lopes et al. 2007; González Delgado et al. 2008; González-Martín et al. 2009; Masegosa et al. 2011). Wolf-Rayet stars (i.e.,"warmers"; Terlevich & Melnick 1985) could successfully mimic the X-ray emission produced by a LLAGN, as well as provide the hard ionizing photons necessary to explain the relative intensities of the observed optical emission lines. If Wolf-Rayet stars were the primary source of ionizing photons for LINER-like emission lines, then most LINERs would be in the immediate post-starburst phase, which is unlikely given their high occurrence rate (Ho et al. 1997b) and stellar populations (Cid Fernandes et al. 2004; González Delgado et al. 2004). Compact starbursts containing hot O stars offer an alternative explanation for the relative intensities of LINER emission lines (Filippenko & Terlevich 1992; Shields 1992), but

* Based on observations made with the NASA/ESA *Hubble Space Telescope*, obtained at the Space Telescope Science Institute, which is operated by the Association of Universities for Research in Astronomy, Inc., under NASA contract NAS 5-26555. These observations are associated with program # HST-GO-12595.
[8] Corresponding author; mem468@psu.edu.

have difficulty explaining the broad Balmer emission wings often seen in LINER spectra (Filippenko 1996), since this would require long-lived supernova remnants. Moreover, the census of stellar populations in LINERs by González Delgado et al. (2004) and Cid Fernandes et al. (2004) does not show a high incidence of compact, nuclear starbursts. pAGB stars and planetary nebulae (Binette et al. 1994; Taniguchi et al. 2000; Yan & Blanton 2012; Belfiore et al. 2016) are more plausible stellar-based models, but are applicable only to a subset of LINERs due to their inability to explain large Hα equivalent widths (Ho et al. 2003). Shock models can adequately describe the off-nuclear optical and ultraviolet (UV) emission-line spectra of some LINERs, such as M87, obtained with the *Hubble Space Telescope* (*HST*; see Dopita et al. 1996, 1997; Sabra et al. 2003). Meanwhile the UV spectra of some LINER nuclei, such as NGC 4579, do not have emission line ratios that are well described by shock excitation, and yet show high ionization lines that would require a hard extreme UV source, such as the continuum from an active galactic nucleus (AGN), or fast shocks (Barth et al. 1996; Dopita et al. 2015). Successful shock models could have a wide range of shock velocities (Filippenko 1996), but the gas must be continuously shocked to maintain LINER-like ratios. The shocks could potentially be driven by radio jets, which are fairly common in LINERs and whose kinetic power is considerably higher than the electromagnetic luminosity of the LLAGNs (Filho et al. 2002; Nagar et al. 2005; Maoz 2007). Alternatively, the shocks could result from supernovae or winds from either young or evolved stars.

LINERs are found in a large fraction of nearby galaxies and the LLAGNs they host define the low-luminosity end of the population of AGNs. Yet none of the models considered above can provide a complete and universal explanation for their energetics. Furthermore, extended LINER-like emission is seen in inactive galaxies observed in the Spectrographic Areal Unit for Research on Optical Nebulae (SAURON), Calar Alto Legacy Integral Field spectroscopy Area (CALIFA), and Mapping Nearby Galaxies at Apache Point Observatory (MaNGA) integral field unit surveys (Sarzi et al. 2010; Papaderos et al. 2013; Singh et al. 2013; Belfiore et al. 2016), in red, inactive galaxies (Yan et al. 2006; Yan & Blanton 2012), and in post-starburst galaxies (Yan et al. 2006; Graves et al. 2007). In these cases the line emission arises over a substantial fraction of the volume of the galaxy and has been attributed to photoionization by pAGB or other old, hot stars. Yan & Blanton (2012) have made the distinction between the original "nuclear" LINERs and these "extended" LINERs while Belfiore et al. (2016) have used the term LIER (low-ionization emission region; *not* nuclear) to describe such galaxies. Thus, we use here the term LINER to denote *compact*, nuclear emission line regions, a few hundred parsecs in size, found in nearby galaxies and the term LIER to refer to large, galaxy-size emission line regions with LINER-like spectra.

Understanding the excitation mechanism of the gas in nearby LINERs is also important for understanding more distant galaxies. Since the LLAGNs in the majority of nearby LINERs do not produce enough ionizing photons to power the emission lines seen on ~100 pc scales, we set out to find indications of other power sources that excite the gas on these large scales. To this end, we obtained spatially resolved spectra of three nearby LINERs with the Space Telescope Imaging Spectrograph (STIS) on the *HST*, spanning the spectral range from the near-ultraviolet (NUV) to the red (Hα). Our goal is to identify and track the energy sources powering the emission lines within the central ~100 pc and determine if different sources dominate on different spatial scales. The STIS spectra have spatial resolution better than 9 pc in three wavelength bands, so we use them to measure emission line ratios as a function of distance from the nucleus. We compare these measurements to physical models for the excitation mechanisms suggested for LINERs, including H II region models (Dopita et al. 2006; Kewley et al. 2006), fast and slow shock models (Shull & McKee 1979; Dopita & Sutherland 1995; Allen et al. 2008), pAGB models (Binette et al. 1994), and AGN photoionization models (Nagao et al. 2002; Groves et al. 2004). In addition to the emission line ratios, we consider the velocity field of the gas, as described by the full width at half maximum (FWHM) and centroid of strong, isolated emission lines. While this work is motivated by the assessment of the photon budget by Eracleous et al. (2010a), we cannot carry out an analogous assessment for mechanical processes, such as shocks, because the models only provide the relative strengths of the emission lines. Therefore our tests here must rely on emission line ratios.

In Section 2 we describe the selection of our targets and summarize their properties. We describe the data and their basic reduction in Section 3, the method for separating the unresolved nuclear source from the extended emission in Section 4, and the subtraction of starlight from the spectra in Section 5. In Section 6 we detail the measurements of the emission lines and in Section 7 we present the inferred temperature and density as a function of distance from the center of each galaxy. In Section 8 we make a detailed comparison of the measured line ratios with physical models. We consider those results and discuss implications for the LINER population in Section 9 and summarize our findings and conclusions in Section 10.

Table 1
Science Targets and Basic Properties

Object (NGC)	z	Distance (Mpc)	CCD Spatial Scale (pc/pix)	MAMA Spatial Scale (pc/pix)	Morphological Type
1052	0.0050[a]	17.8[b]	4.31	2.16	E4
4278	0.0023[a]	14.9[c]	3.61	1.81	E1–2
4579	0.0050[d]	16.8[e]	4.07	2.04	SBb

Notes.
[a] Redshift from van Velzen et al. (2012).
[b] Distance from Tully (1988); in agreement with the surface brightness fluctuation method (see Jensen et al. 2003).
[c] Distance from the surface brightness fluctuation method (see Jensen et al. 2003).
[d] Redshift from Falco et al. (1999).
[e] Distance from Tully (1988); in agreement with the tip of the red giant branch method (see Tully et al. 2013).

2. Experimental Design and Target Selection

To diagnose the excitation mechanisms of the emission line gas and their relative importance on small scales around the nuclei of our target galaxies, we obtained long-slit spectra with the *HST*/STIS. By covering the spectral range from the NUV (~1900 Å) to the red (~6800 Å), we measured both well known diagnostic line ratios such as [O III]/Hβ, [N II]/Hα and [O I]/Hα, as well as a number of optical lines that are good probes of shocks, such as [Fe XIV] λ5303, and [Fe X] λ6374. We also looked for [Ne IV] λ2423, an NUV line that is also a

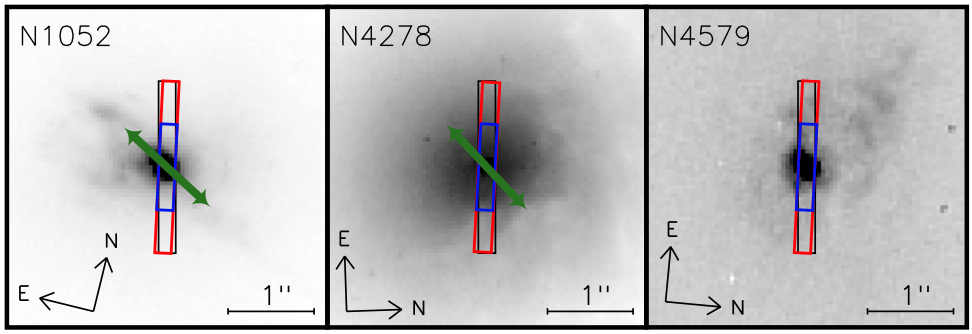

Figure 1. Images with slit and approximate jet orientation superposed for the three objects studied in this paper. The black (vertical) rectangle shows the slit placement of the original red (Hα) observation from Walsh et al. (2008). The red (slightly rotated, full length) and blue (slightly rotated, half length) rectangles show the slit placement for the blue (Hβ) and NUV observations, respectively. See Section 3 for a more detailed discussion on the observations. The length of each rectangle represents the physical extent to which we could detect emission lines in each wavelength band. The green arrows show the direction of the radio jets in each object (length not to scale). The radio morphologies of all three objects are described in Section 2. Left: NGC 1052 in a narrow band around the Hα+[N II] $\lambda\lambda$6548, 6583 lines with the WFPC2 F658N with the small-scale jet orientation shown by the green arrows, see Section 2 for details. Center: NGC 4278 in a wide continuum band with the WFPC2 PC F555W. Right: NGC 4579 in the same band as NGC 1052.

good probe of shocks. This line was detected in NGC 1052 by Dopita et al. (2015), but we were not able to detect it in our NUV spectra because of their lower signal-to-noise ratio (S/N).

We selected as our targets the three galaxies listed in Table 1, based on the following criteria: (1) a deficit of ionizing photons from the LLAGN as described in Eracleous et al. (2010a), (2) multiple indicators for the presence of an AGN, and (3) existing archival Hα spectra from *HST*/STIS (Walsh et al. 2008) that we could use to make our observing program economical. Moreover, Walsh et al. (2008) studied the velocity field of the line-emitting gas in our three target galaxies using these spectra, and we take advantage of their results in our interpretation of all the data.

Our targets include NGC 4278, which has a severe ionizing photon deficit, and NGC 4579, for which photoionization from the LLAGN is plausible only if all the ionizing photons are absorbed by the line-emitting gas (Eracleous et al. 2010a). We also targeted NGC 1052, for which emission line imaging (Pogge et al. 2000) and X-ray spectroscopy (Brenneman et al. 2009) show the nucleus is likely obscured along some lines of sight, suggesting that the AGN cannot be the only power source. Furthermore, previous observations of NGC 1052 with the Faint Object Spectrograph on the *HST* by Gabel et al. (2000) show shock-excited NUV emission lines.

All three targets have radio emission. NGC 4278 has compact jets, with a length of 0.″015 (1.2 pc) in the 6 cm band (Giroletti et al. 2005; Helmboldt et al. 2007). NGC 4579 has an unresolved radio core that is smaller than 0.″0025 (<0.2 pc) in the 5 GHz band (Falcke et al. 2000). NGC 1052 has a pair of large jets, each of length 15″ (1.3 kpc) in the 20 cm band (Jones et al. 1984; Wrobel 1984), as well as resolved jets on smaller scales of length 0.″008 (0.7 pc) in the 2 cm band (Claussen et al. 1998; Kellermann et al. 1998). The small- and large-scale jets in NGC 1052 show a change in position angle, from approximately 60° to 95° as described in Claussen et al. (1998). Because of the spatial scales probed by our observations, we consider the small-scale jet to be the most relevant to our discussion; hence we will refer to the small-scale radio jet of NGC 1052 as "the jet" hereafter.

In Figure 1 we show *HST* images of the targets covering a region of a few arcseconds in size around the nucleus. The directions of the resolved, smaller-scale radio jet of NGC 1052 and the radio jet in NGC 4278 are also marked in these images.

3. Observations and Basic Data Reduction

We obtained new Hβ-region optical (hereafter, "blue") and NUV long-slit spectra of the targets in 2012 May using the charge-coupled device (CCD) and NUV-Multi-Anode Microchannel Array (NUV-MAMA) detectors of STIS, respectively, employing the 52″ × 0.″2 slit. We supplemented these data with archival Hα (hereafter, "red") spectra obtained in 1999 and 2000 through the same slit with the STIS CCD and G750M grating, and presented by Walsh et al. (2008). The physical separation between the spectra along the slit for each galaxy and detector are listed in Table 1, and the log of observations is given in Table 2. We used the same slit position angle for the new observations taken with the CCD and NUV-MAMA detectors.

The archival spectra cover the wavelength range 6300–6860 Å with a scale of 0.″05 pixel^{-1} along the slit and a dispersion of 0.56 Å pixel^{-1}. The blue spectra were taken with the CCD detector and the G430L grating, covering a wavelength range of 2900–5700 Å with a scale of 0.″05 pixel^{-1} along the slit and a dispersion of 2.73 Å pixel^{-1}. The NUV spectra were taken with the NUV-MAMA detector and the G230L grating, covering a wavelength range of 1570–3180 Å with a scale of 0.″025 pixel^{-1} along the slit and a dispersion of 1.58 Å pixel^{-1}. The slit alignment of the new data compared to the archival observations, as well as the jet orientations for NGC 1052 and NGC 4278, are shown in Figure 1.

In the new CCD observations we placed the object near the readout amplifier and took multiple exposures for the blue spectra to reduce the effects of charge transfer inefficiency on the resulting images. To further mitigate these effects, as well as the effect of cosmic rays, we used the STIS-ALONG-SLIT dither pattern where each exposure was linearly offset by three pixels in the spatial direction, corresponding to a 0.″15 shift between CCD exposures and a 0.″075 shift between NUV-MAMA exposures.

Each raw 2D spectral image, including the archival red spectra, was processed through the `calstis` pipeline. Before the final step in the pipeline, we removed most of the hot pixels and cosmic rays in our blue and red spectral images using the routine `L.A. Cosmic` (van Dokkum 2001). The NUV spectral images were not processed through `L.A. Cosmic` as the NUV-MAMA detector is not affected by cosmic rays. To account for the dither pattern, we shifted the images to realign

Table 2
Summary of New Observations of Science Targets

Object (NGC)	Spectrum Observed	Instrument Used	Wavelength Range (Å)	Position Angle (°E of N)	UT Date	Number of Exposures	Exposure Time (s)
1052	red (Hα)	STIS/CCD	6300–6860	13.8	1999 Jan 02	1	1974
	blue (Hβ)	STIS/CCD	2900–5700	11.1	2012 Nov 29	6	4407
	NUV	STIS/NUV-MAMA	1570–3180	11.0	2012 Dec 06	4	10736
4278	red (Hα)	STIS/CCD	6300–6860	88.0	2000 May 11	1	3128
	blue (Hβ)	STIS/CCD	2900–5700	85.1	2012 May 20	6	4437
	NUV	STIS/NUV-MAMA	1570–3180	85.0	2012 May 20	2	6014
4579	red (Hα)	STIS/CCD	6300–6860	95.4	1999 Apr 21	1	2692
	blue (Hβ)	STIS/CCD	2900–5700	92.5	2012 May 19	6	4425
	NUV	STIS/NUV-MAMA	1570–3180	92.4	2012 May 19	2	5990

Table 3
Summary of Observations of PSF Stars

Object	Spectrum Observed	Instrument Used	Wavelength Range (Å)	UT Date	Exposure Time (s)
Sirius B	red (Hα)	STIS/CCD	6300–6860	2004 Feb 06	90
BD+75D325	blue (Hβ)	STIS/CCD	2900–5700	2000 Aug 10	29
GRW+70D5824	NUV	STIS/NUV-MAMA	1570–3180	1997 Oct 31	150

them using the IRAF[9] task imshift, and used the IRAF task imcombine to median combine the aligned images, adopting the standard deviation from individual exposures as the error bar for each pixel in the resulting 2D spectrum. The archival red spectra consisted of a single exposure for each galaxy, so this last step was not carried out.

We found that the rectification of the curvature of the 2D spectrum, carried out by calstis, left an unacceptably large residual curvature, so we applied an improved geometric rectification. We fitted a low-order polynomial to the spatial peak position as a function of location along the dispersion direction in all the final 2D spectra. We chose the lowest-order polynomial that ensured that, after the fit was subtracted from the data, the position of the spatial profile peak was both constrained within a tenth of a pixel along the slit, and showed no systematic trend in the dispersion direction. Following this correction, we proceeded to the scientific analysis of the 2D spectra, as we describe in the following sections.

4. Separating Resolved and Unresolved Light in the 2D Spectra

All three of our objects have multiple indicators of the presence of an AGN, including broad emission lines in their nuclear spectra obtained with STIS. Thus, we searched for and removed any contribution from the bright unresolved nuclear source in the rows of the 2D spectra near the nucleus. By taking this measure, we separated the spatially unresolved nuclear source in each band from the extended, resolved source.

4.1. Fitting Method

To separate the two spatial components, we modeled the light profiles of each wavelength bin in each 2D spectrum as a broad base from the extended, resolved light with a strongly peaked, unresolved core. We adopted the Nuker law to describe the resolved starlight (Lauer et al. 1995), under the assumption that a substantial portion (but not necessarily all) of the emission line flux follows the distribution of the starlight. For the strong, unresolved core (i.e., the AGN), we parameterized the point-spread function (PSF) of the instrument by fitting the spatial profiles of stars observed with the same instrument configuration as the 2D spectrum with a combination of two Gaussians for the red and NUV spectra and three Gaussians for the blue spectra. A log of the archival observations of the stars we used is given in Table 3. The final spatial model thus consists of a linear combination of a Nuker model, which describes both the stellar continuum and light from any other source that follows the spatial distribution of the starlight, and a pointlike central component modeled using the PSF, which describes the light from the unresolved nuclear source. Fits to the stellar continuum of individual spectra extracted from different distances from the center of a galaxy are carried out at a later stage in the analysis, as detailed in Section 5. We allowed the fitting routine to underfit but not overfit each spatial profile in spectral pixels with emission lines.

We fitted the spatial model to the spatial profile along each column of a 2D spectrum (i.e., at each wavelength). Our procedure involved binning the model to match the detector pixels before comparing it to the flux in the 39 central pixels of the observed spatial profile. The total model is described by a total of eight free parameters; six parameters are needed for the Nuker model (the five parameters in Equation (3) of Lauer et al. 1995, plus a shift) and two for the PSF (amplitude and shift). We did not convolve the Nuker model with the PSF of the instrument since we were able to achieve our primary goal of fitting the inner parts of the spatial profile equally well with and without such a convolution.

The rationale behind our spatial modeling was that the extended *line* emission could be described by a Nuker law plus positive deviations that represent clumps of emission line gas and is justified by the emission line morphologies revealed by narrow band images (e.g., Pogge et al. 2000). Moreover, our primary goal is to identify the contribution of the unresolved

[9] IRAF is distributed by the National Optical Astronomy Observatories, which are operated by the Association of Universities for Research in Astronomy, Inc., under cooperative agreement with the National Science Foundation.

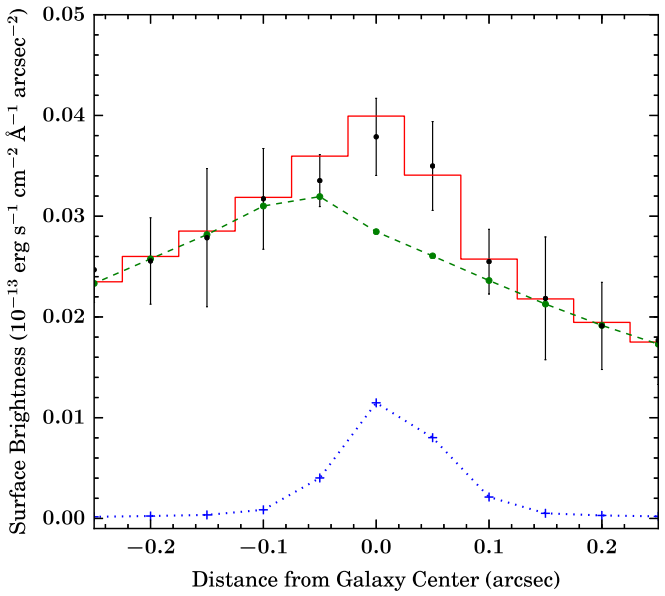

Figure 2. Example of a fit to the spatial profile at a wavelength of 5106.5 Å in the blue spectrum of NGC 1052, where the light is dominated by the continuum. The data are shown as black points with error bars, the blue "+" signs connected by the dotted blue line represents the binned PSF model, and the binned Nuker model is shown as green dots connected by a dashed line. These are both intrinsically symmetric but may appear asymmetric after binning. The two model components are added together to get the total model, represented by the red histogram. Our requirement for a good fit is that the model is either within or below the error bars at all points. The Nuker model and PSF model do not have the same peak position, but it is within the accepted separation as described in Section 4.1.

nuclear source to the light profile and remove it, and then ascribe what is left in the light profile to extended emission.

We applied this fitting method to each 2D spectrum separately. The exact centroids of the two components of the model were allowed to vary within two pixels of each other (the uncertainty associated with the location of the PSF in each wavelength bin).

In Figures 2 and 3 we show examples of fits to the spatial profiles at a continuum and an emission line wavelength, respectively. In each figure we compare the binned model to the data and we also show the components that make up the model, after binning them. In Figure 2, the best-fitting Nuker component appears asymmetric as a consequence of binning it before comparing it with the data. The intrinsic Nuker component is symmetric but has a sharp core that falls near the boundary between two spectral bins. Once the best fit was obtained, we used the resulting PSF model to subtract the contribution of the unresolved source from each spectral pixel and isolate the extended emission. We also integrated the PSF flux in each spectral pixel to obtain the spectrum of the unresolved nuclear source. At the end of the fitting process, we examined the spectra to ensure that broad emission lines were detected only in the spectrum of the unresolved source. Below we give specific notes for each object and present an example of the outcome.

NGC 1052. We successfully decomposed the spatially unresolved nuclear source and the extended, resolved sources in all three spectral bands for NGC 1052. Figure 4 shows the outcome of this decomposition for a spectrum located four rows from the nucleus. As expected, the Nuker law spectrum follows the starlight continuum, while the PSF model spectrum contributes only to the emission lines. The broad lines are successfully isolated in the NUV and blue spectra of the spatially unresolved nuclear source.

The Hα emission line in the spectrum of the central region (central row) of the extended emission has broad wings. It is possible that there is some residual contamination of this spectrum from light from the unresolved nuclear source (the measurements from this row are labeled with a "c" in the diagnostic diagrams presented in Section 8). However, it is also possible that the broad emission we detect here represents scattered light within the galaxy (not the telescope or instrument optics) from the spatially unresolved nuclear source. The latter interpretation is supported by the fact that Barth et al. (1999) found that the broad Hα wings in NGC 1052 are preferentially polarized, suggesting a substantial contribution from scattered light. We also note that we further constrained the Nuker profile to vary smoothly near the peak of the emission lines, i.e., a range of ∼5–10 Å bracketing the peaks of the emission lines, in the red spectrum of NGC 1052 in order to obtain a good fit at the line peak. Figure 3 shows an example of such a spatial profile fit.

NGC 4278. We found only tentative evidence of spatially unresolved nuclear light in the blue and red spectra. A good fit was also possible with a model that included no unresolved source. Moreover, the only viable fit to the NUV spectrum did not include an unresolved source. Therefore, in the rest of the analysis we assume that there is no detectable unresolved source in NGC 4278.

NGC 4579. The spatially unresolved nuclear source in NGC 4579 is so bright that we were not able to completely remove its contribution to the resolved light in the red and blue bands. The central blue spectrum of the resolved source exhibits wings on the Hβ emission line, presumably a result of residual light from the unresolved nuclear source. Similarly, in the red band we were not able to separate the resolved and unresolved sources in the central pixels. The contamination of the resolved light by the unresolved source is confined to two rows around the nucleus. We found that the NUV spectrum is dominated by light from the unresolved nuclear source, as illustrated in Figure 5: the blue spatial profile is sharply peaked with broad wings from the resolved light, but the NUV spatial profile only has a sharp peak and almost exactly matches the PSF template.

4.2. Assessment of the Spatial Decompositions and Discussion of Uncertainties

We reiterate the cautionary notes about the results of the spatial decomposition at ±2 pixel rows from the nucleus of NGC 4579. As we describe in later sections, we add together pairs of pixel rows to obtain spatially resolved 1D spectra, which implies that the spectra of the resolved emission of NGC 4579 in the two spatial bins closest to the nucleus (±8 pc from the center) are not useful for our later analysis. A similar caution applies to the red spectrum of the innermost spatial bins in NGC 1052 (±4.3 pc from the center). We consider the results of the spatial decomposition at larger distances from the nuclei of these two galaxies reliable because the PSF contribution drops by nearly an order of magnitude at three

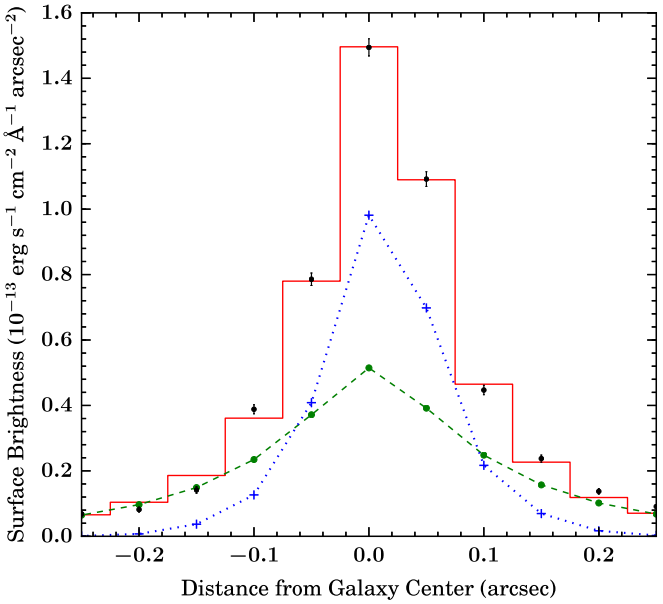

Figure 3. Example of a fit to the spatial profile at a rest wavelength of 6559.3 Å in the red spectrum of NGC 1052, where the light is dominated by the Hα emission line. Here, the S/N is considerably higher than the continuum column shown in Figure 2 and the contribution from the unresolved nuclear source is comparable to that of the resolved emission at the center of the galaxy. The data are shown as black points with error bars, the blue "+" signs connected by the dotted line represents the binned PSF model, and the binned Nuker model is shown as green dots connected by a dashed line. These are both intrinsically symmetric but may appear asymmetric after binning. The two model components are added together to get the total model, represented by the red histogram. See detailed discussion in Section 4.1.

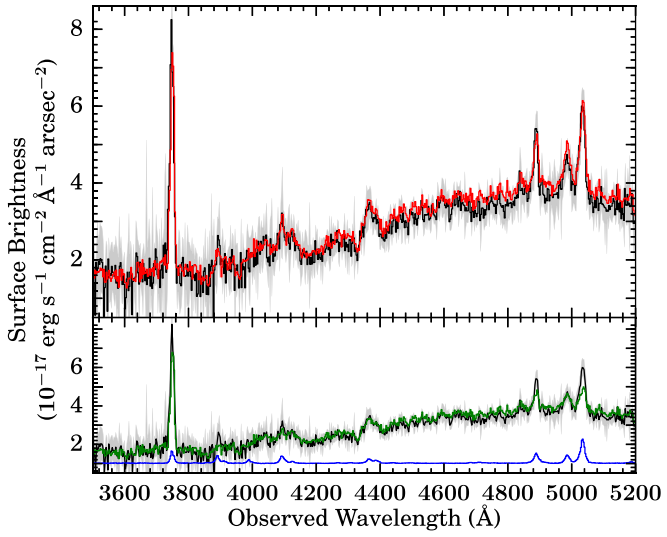

Figure 4. Example of the decomposition of a blue spectrum for NGC 1052 into spectra of the resolved and unresolved light. The spectrum was extracted from a region four rows away from the nucleus. The data and errors are represented by the black solid line and gray shaded region, respectively. The red line in the top panel shows the total model. The blue (emission lines with no continuum) and green (emission lines with continuum) lines in the bottom panel show the contribution of the unresolved light and the Nuker model, respectively. The Nuker model accurately captures the starlight continuum and some of the emission line flux, while the unresolved light only contributes significantly in the emission lines. See detailed discussion of the fitting process in Section 4.1.

pixels from the peak and and becomes lower than the contribution of the resolved light (see Bowers 1997, and Figures 2 and 3 of this paper).

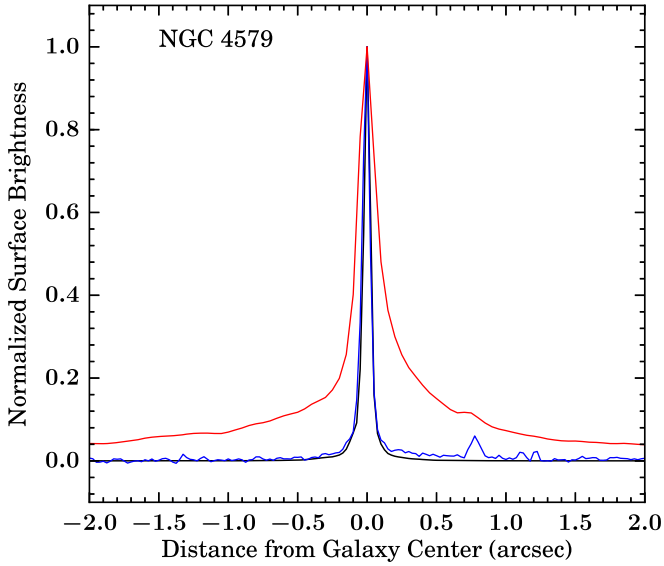

Figure 5. Comparison of the spatial profiles of NGC 4579. We show the NUV spectrum (at 2962.6 Å) in blue (noisy narrow profile), the blue spectrum (at 5340.7 Å) in red (smooth broader profile), and the NUV stellar PSF template (integrated from 1570 to 3180 Å) in black (smooth narrow profile). We choose the blue spectrum for this comparison as it has clearly detected resolved emission. The spatial profiles are in units of erg s^{-1} cm^{-2} Å^{-1} arcsec^{-2} and normalized to unit maximum. The NUV spatial profile does not have the broad wings that appear in the blue spatial profile, but instead looks almost identical to the stellar PSF, implying the NUV spectrum is dominated by the light from the unresolved nuclear source. See Section 4.1 for more details.

To assess further the robustness of the spatial decomposition, we checked whether the spectra of the unresolved sources in NGC 1052 and NGC 4579 in the three different bands connect smoothly to each other. Thus, we fitted a simple power-law model (a very common description of AGN optical continua, e.g., Vanden Berk et al. 2001) to continuum windows in the three spectra of each object. This approach is further justified by the fact that we observe broad emission lines and no stellar absorption lines in the spectrum of the unresolved sources of both galaxies (we quantify the contribution of starlight in Section 5 below). We found that the continua in all three bands are indeed described by a common power-law model and that the post-fit residuals have a Gaussian distribution about zero. To estimate the uncertainty in the relative normalization of the three individual spectra of each object, we explored how much the normalization of each of the three spectra can be changed while still keeping the distribution of residuals from that spectrum within one standard deviation ("1σ") from zero. Thus we found normalization uncertainties of $\pm$74%, $\pm$41%, $\pm$37% for the NUV, blue, and red spectra of NGC 1052 and $\pm$12%, $\pm$12%, and $\pm$10% for the corresponding spectra of NGC 4579. The magnitude of the uncertainties depends directly on the strength of the continuum in each band; it is highest for the NUV spectrum of NGC 1052 where the continuum is fairly weak. This uncertainty affects only ratios of lines that are detected in different spectra taken with different gratings and only when the spectra are within $\pm$2 pixel rows from the nucleus where the contribution of the PSF is substantial. It is taken into account in later error calculations for the emission line strengths measured from the spectra of the unresolved and resolved sources of these galaxies. We return to this issue in Section 6.4 where we discuss how this uncertainty affects our estimates of extinction.

5. Subtraction of Starlight from the Extracted 1D Spectra

5.1. Fitting Method

After removing the contribution of the spatially unresolved nuclear source, we extracted 1D spectra from each row of the extended (and resolved) 2D spectrum of each galaxy as a function of distance from the nucleus along the slit. The spectra of the resolved light include starlight, while the spectra of the unresolved nuclear source in NGC 1052 and NGC 4579 have continua dominated by non-stellar light from the AGN and a contribution from starlight. We used the Penalized Pixel-Fitting code pPXF (Cappellari & Emsellem 2004) to fit the total continuum in each 1D spectrum and isolate the emission lines. Our primary goal was to isolate the emission lines and not to determine the properties of the continuum. Therefore, we sought good fits to portions of the continuum where absorption lines are present but did not thoroughly explore the parameter space of stellar continuum models.

We adopted the stellar population synthesis models (known as simple stellar population, or SSP, models) from the MILES database (Sánchez-Blázquez et al. 2006) for both the blue and red spectra, and the Bruzual & Charlot (2003, BC03) UV stellar models for the NUV spectra. pPXF requires the same wavelength sampling for the input spectra and stellar templates. The MILES library allows for user-defined wavelength sampling, but the spectra it includes only cover a wavelength range of ∼3500–7400 Å. Therefore, we created the NUV stellar continuum templates by rebinning the BC03 models to match the wavelength scale of the observed NUV spectra. We assumed a Salpeter initial mass function for both sets of models, the Padova 2000 isochrones (Girardi et al. 2000) for the MILES SSP models, and the Padova 1994 evolutionary tracks (Bertelli et al. 1994) for the BC03 models. The free parameters of both the MILES SSP models and BC03 models are the metallicity Z (0.02–1.6 $Z_\odot$ for MILES, 0.005–2.6 $Z_\odot$ for BC03) and population age (0.06–17.8 Gyr for MILES, 0–20 Gyr for BC03). We used a power law to model the continuum of the AGN in the 1D unresolved nuclear spectra of NGC 1052 and NGC 4579. The starlight and power-law continuum models were combined after weighting each by a low-order multiplicative polynomial to account for any change to the overall shape of the continuum caused by extinction. All required components were fitted simultaneously by pPXF.

5.2. Fitting Results and Evaluation of Uncertainties

Figure 6 shows an example of a fit to a single spectrum extracted from NGC 4579. The upper panel shows the fit and the residual spectrum, and the lower panel shows scaled versions of all the templates used in the fit. While each galaxy required a different combination of stellar population ages, all three galaxies were best fitted with the largest value of metallicity for the given family of models as judged from the slope of the underlying stellar continuum.

The spectra of NGC 1052 were well fitted by combining 2 and 10 Gyr stellar population models with a low-order multiplicative polynomial. While all spectra required the 10 Gyr population to accurately describe the starlight, the 2 Gyr population was included only when necessary, and with no discernible trend as a function of distance from the nucleus. We also used a power-law continuum in the NUV and blue spectra of the unresolved nuclear source in NGC 1052.

The spectra of NGC 4278 were also well fitted by combining 2 Gyr and 10 Gyr stellar population models with a low-order multiplicative polynomial. The 10 Gyr population was required at all distances from the nucleus, while the 2 Gyr population was used most heavily near the nucleus. There was no detected unresolved nuclear source, and no power law required for the fit. The spectra of NGC 4579 required 2, 3, 6, and 10 Gyr stellar populations and a low-order multiplicative polynomial, with no trend in population age with distance from the nucleus. A power law was included in the model for the blue spectrum of the unresolved nuclear source.

We bootstrapped our best-fitting continuum model to calculate the error spectrum associated with it. Specifically, we simulated 1000 spectra by perturbing each data point according to its associated error bar, and repeated the fitting process using the parameter values found in the best-fitted continuum model as input parameters. The distribution of resulting model parameters was Gaussian and we took the standard deviation of this distribution as the error on the parameters of the continuum fit. This process was carried out for each extracted 1D spectrum, as well as the unresolved 1D spectrum, for all three galaxies. We incorporated the error bars from this exercise in our error propagation calculations.

6. Emission Line Spectra and Measurements

6.1. Presentation and Qualitative Discussion of Spectra

A subset of the final spectra that we used in our analysis are shown in Figures 7 through 19, where they are presented without extinction corrections. We combined the spectra of the resolved light in pairs of two for our analysis because the PSF of each instrument is approximately two pixels wide, which means that adjacent spectra are not independent. We obtained the nuclear spectrum of the extended, resolved light by combining the two 1D spectra that bracket the peak of the spatial profile.

The spectra of the three objects exhibit different qualitative behaviors as a function of distance from the nucleus, as described below.

NGC 1052. The spectrum of the unresolved nuclear source shows broad Hα, Hβ and Mg II $\lambda\lambda$2798, 2803 lines as well as optical Fe II blends in the vicinity of Hβ. The NUV spectra of the extended resolved light have detectable emission lines only within 40 pc. In the blue spectra, the strength of the [O III] λ5007 line declines faster with distance from the nucleus than that of the [O II] λ3727 line. Hα and [N II] $\lambda\lambda$6548, 6583 are the strongest lines in the red spectra of the extended resolved light, and are detected to distances of up to 80 pc.

NGC 4278. The NUV spectra of the extended resolved light have detectable emission lines only within the central 18 pc. The relative intensities of the lines in the blue spectra of the extended, resolved light do not vary significantly as a function of distance from the nucleus. The Hα and [N II] $\lambda\lambda$6548, 6583 lines are stronger than the [S II] $\lambda\lambda$6716, 6731 doublet at and near the nucleus but their relative strengths change with distance from the nucleus and become comparable by 29 pc from the nucleus.

NGC 4579. The NUV spectrum is dominated by the spatially unresolved nuclear source with no discernible contribution from extended emission, hence Figure 7 shows the integrated NUV spectrum. The [O III] λ5007 line declines

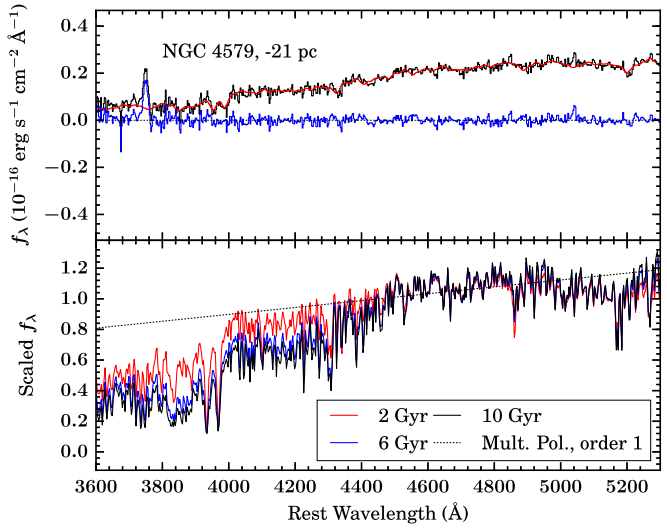

Figure 6. Example of the stellar continuum fit to a spectrum extracted from a distance of approximately 21 pc from the nucleus of NGC 4579. The top panel shows the observed spectrum in black, the continuum fit in red, and the residual spectrum in blue. The bottom panel shows the components of the model continuum: a multiplicative polynomial of order one (dotted line) and the 2, 6, and 10 Gyr stellar populations (red, blue and black lines; listed in order of continuum strength around the Ca II H & K $\lambda\lambda$3969, 3934 lines), scaled to match at 4700 Å. See the detailed discussion in Section 5 of the text.

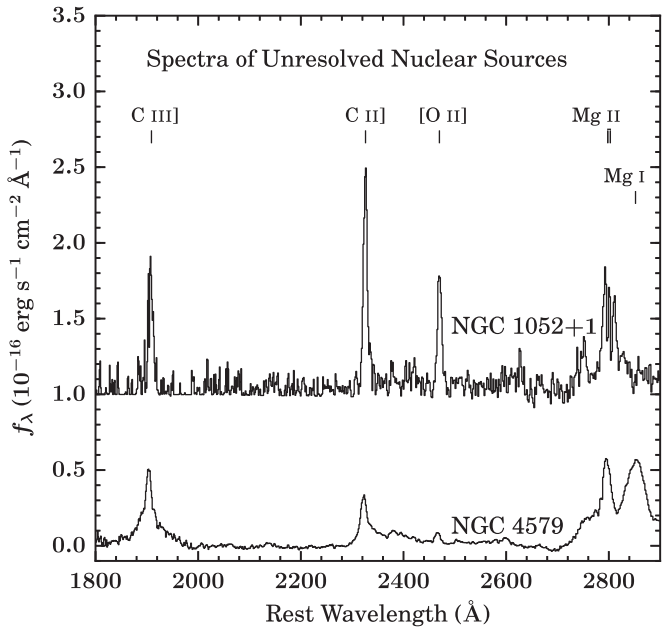

Figure 7. NUV spectra of the spatially unresolved nuclear sources in NGC 1052 and NGC 4579. The spectra are offset vertically from each other for clarity, by the offsets given in the figure. The prominent emission lines are marked and labeled. NGC 4579 shows no resolved nuclear emission in this band, so the spectrum presented here is the spatially integrated spectrum. Both objects show broad Mg II emission lines, indicative of an AGN. See Section 6 for a detailed discussion of Figures 7 through 19.

in strength faster than the [O II] λ3727 line with distance from the nucleus. The unresolved nuclear source dominates and overwhelms any resolved emission in the red spectra in the vicinity of the nucleus. Therefore, the red spectra of the extended, resolved light shown in Figure 17 start at 12 pc from the nucleus. Hα and [N II] $\lambda\lambda$6548, 6583 are the strongest lines in the red spectra of the extended, resolved light, detected out to 80 pc. The NUV and blue spectra of the unresolved nuclear source also show Fe II and Fe III complexes that are characteristic of AGN spectra. These complexes are also evident in the central blue spectrum of the resolved emission, which is contaminated by light from the unresolved nuclear source.

We also present synthetic integrated spectra through a larger aperture in the blue and red bands, which include both the unresolved and resolved light. The results of this exercise are shown in Figures 18 and 19. The synthetic spectra represent the emission from a circle centered on the nucleus with a radius of

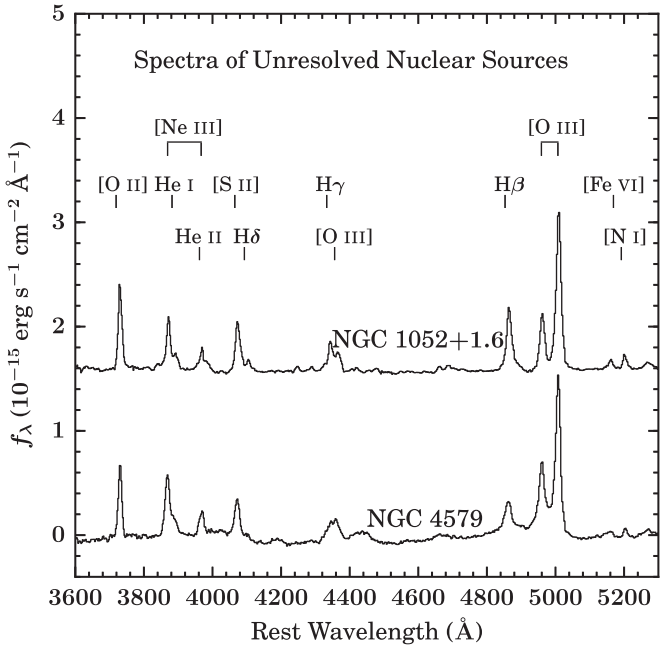

Figure 8. Same as Figure 7, for the blue spectra. NGC 4579 has broad Balmer emission lines indicative of an AGN.

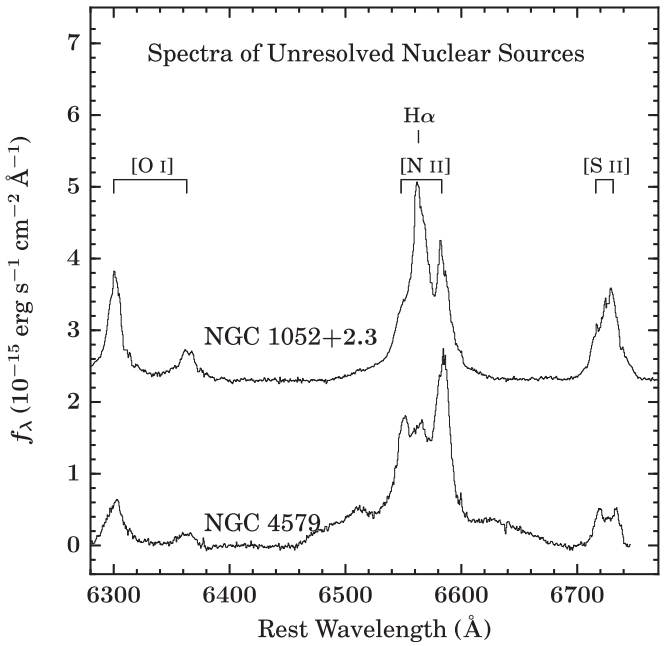

Figure 9. Same as Figure 7, for the red spectra. Both objects show broad Balmer emission lines indicative of an AGN.

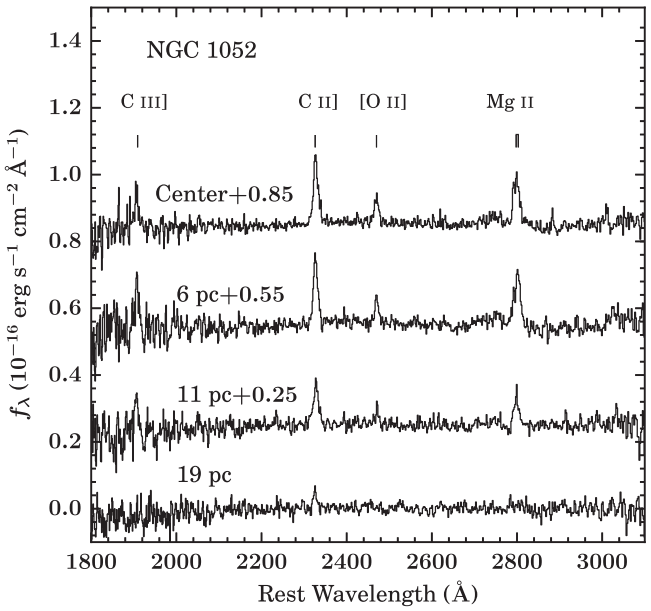

Figure 10. NUV spectra of the extended, resolved source in NGC 1052 at various distances moving outward from the nucleus. The spectra are offset vertically from each other for clarity, by the offsets given in the figure. The prominent emission lines are marked and labeled. The C III] λ1909 line can be difficult to detect and measure because of the noise at the blue end of the spectra.

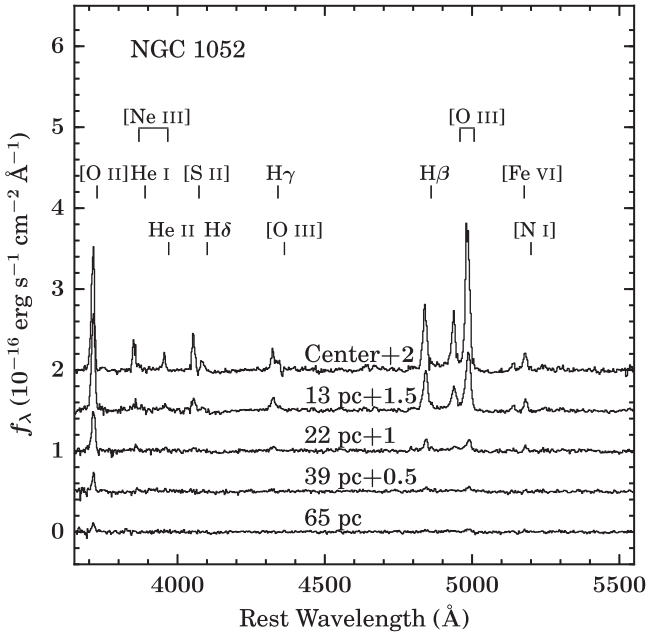

Figure 11. Same as Figure 10, for NGC 1052, blue spectra. The [O II] λ3727 line is seen over the greatest spatial extent; it becomes stronger than the [O III] λ5007 line at 12 pc from the nucleus.

1″, i.e., the expected LINER-like spectrum from a ground-based observation. They were produced via a weighted sum of observed spectra at different distances from the galaxy center with weights chosen according to the area of an annulus at that distance from the center. The simulated spectra also approximate those we expect from a 2″ × 4″ rectangular slit used in some of the well known surveys of LINERs (e.g., Phillips et al. 1986; Ho et al. 1997a). Both the blue and red integrated spectra are reminiscent of the characteristic LINER spectrum.

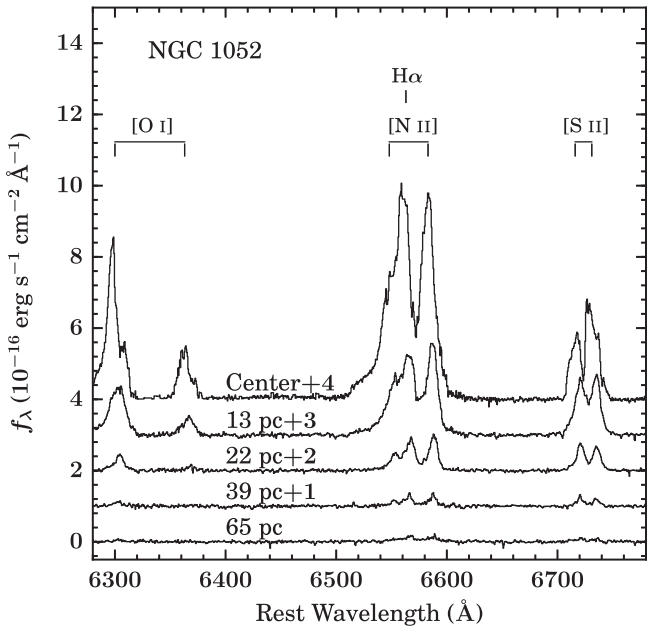

Figure 12. Same as Figure 10, for NGC 1052, red spectra.

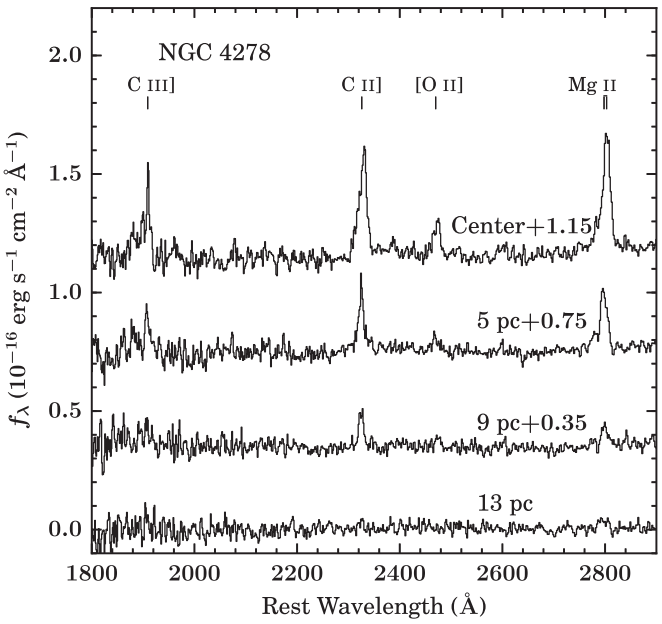

Figure 13. Same as Figure 10, for NGC 4278, NUV spectra. The excess noise at the blue end of the spectrum makes C III] λ1909 difficult to detect past 5 pc from the center.

All three objects have significantly stronger [O II] λ3727 emission compared to [O III] λ5007 in their integrated blue spectra. Moreover, the broad Balmer lines from the nuclei of NGC 1052 and NGC 4579 are diluted so that only a weak broad Hα pedestal is discernible.

6.2. Measurement of Emission Line Strengths

We measured the emission line fluxes using the `iraf` task `specfit` (Kriss 1994), which fits the line profiles with linear combinations of Gaussians by minimizing the χ^2 statistic using

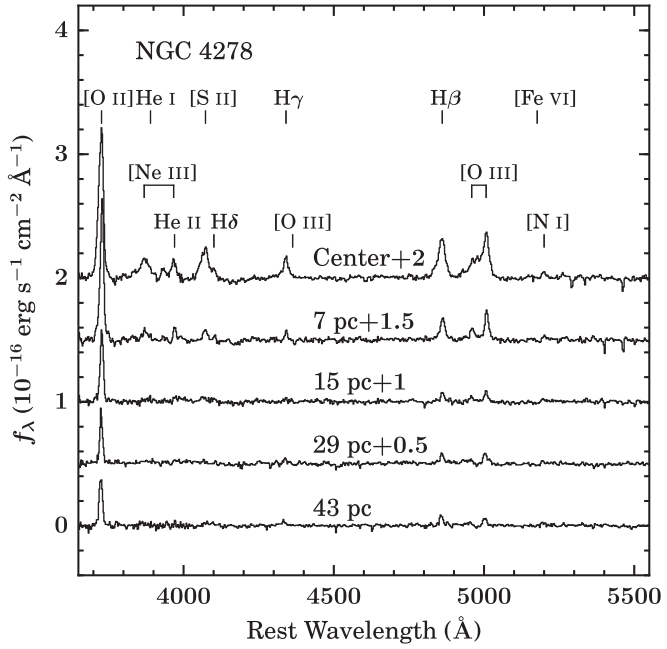

Figure 14. Same as Figure 10, for NGC 4278, blue spectra. The [O II] λ3727 line is stronger than the [O III] λ5007 line at all distances.

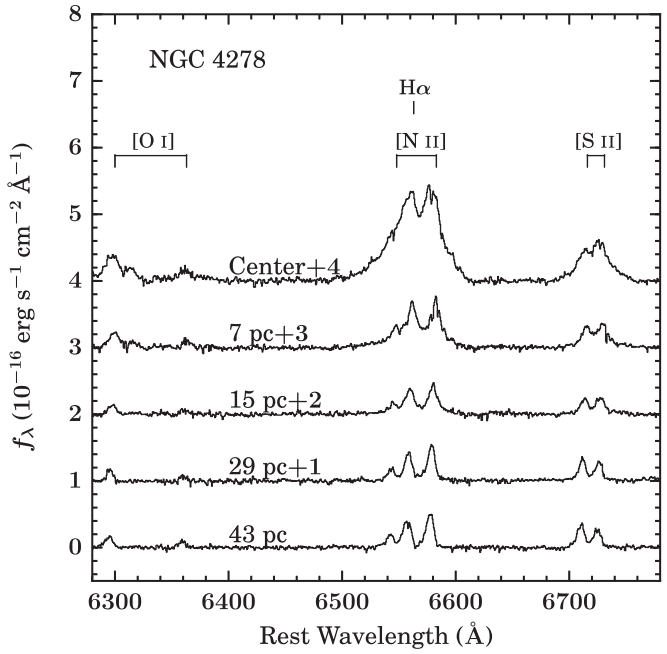

Figure 15. Same as Figure 10, for NGC 4278, red spectra.

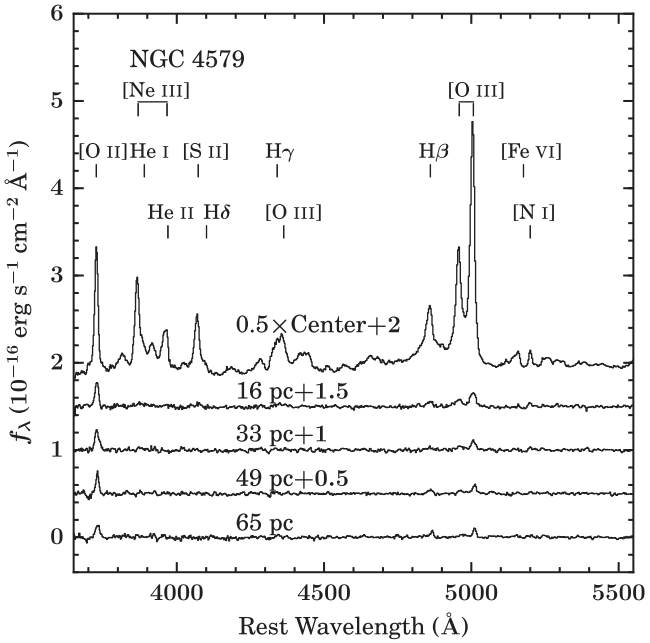

Figure 16. Same as Figure 10, for NGC 4579, blue spectra. The central spectrum is scaled by 0.5 for easier comparison with the other spectra. [O II] λ3727 is seen at the greatest spatial extent, and becomes stronger relative to [O III] λ5007 at 16 pc from the nucleus.

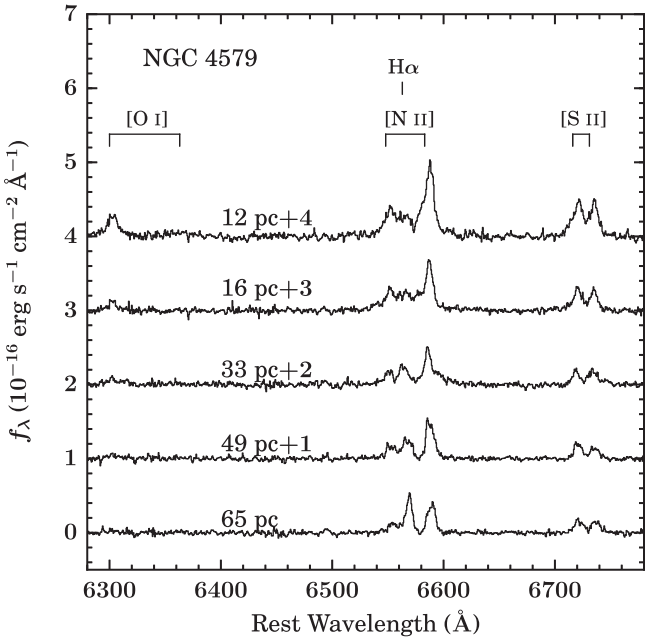

Figure 17. Same as Figure 10, for NGC 4579, red spectra. We do not detect resolved emission in the nucleus of the galaxy because of the strength of the unresolved emission.

the simplex method. We also inspected the fit and the post-fit residuals to make sure they had no systematic patterns. We regard the Gaussian components only as a means of parameterizing the line profiles and do not attach any particular physical significance to them. Near the nuclei of NGC 1052 and NGC 4579, we modeled any detected Fe II and Fe III emission with optical Fe II templates from Boroson & Green (1992) for the blue spectra, and NUV Fe templates from Vestergaard & Wilkes (2001) for the NUV spectra. The spectra of both the spatially unresolved nuclear sources and the central region of the extended, resolved sources in NGC 1052 and NGC 4579 have broad lines which we fitted simultaneously with the narrow lines. We show an example of a narrow line only fit in Figure 20 and an example of a fit with both broad and narrow lines in Figure 21. We report the measurements (without any extinction corrections) in Tables 4–8.

We constrained the widths of lines in doublets, namely Mg II $\lambda\lambda$2798, 2803, [O III] $\lambda\lambda$4959, 5007, [O I] $\lambda\lambda$6300, 6363, [N II] $\lambda\lambda$6548, 6583, and [S II] $\lambda\lambda$6716, 6731 to be equal. We also imposed the corresponding physical flux ratio on the above doublets as follows: no constraint on [S II] $\lambda\lambda$6716, 6731 since the ratio depends on the density, $1/$

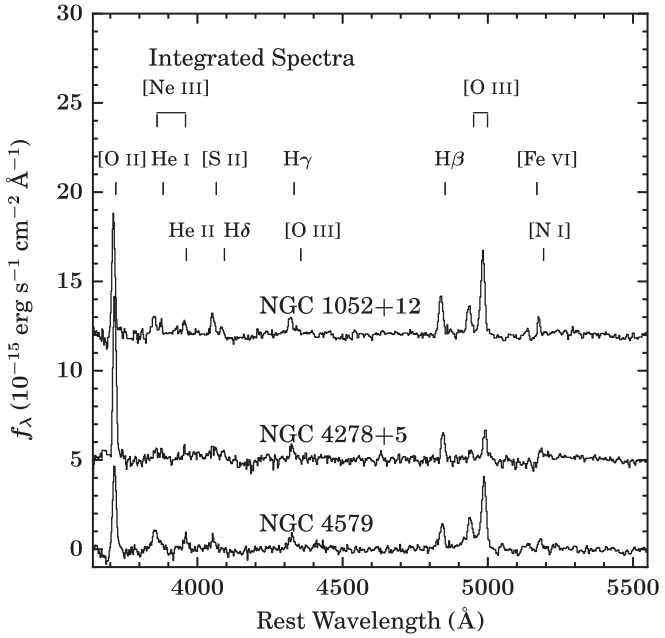

Figure 18. Same as Figure 7, for integrated blue spectra, constructed as described in Section 6.1. The [O II] λ3727 line is significantly stronger than the [O III] λ5007 line in all objects.

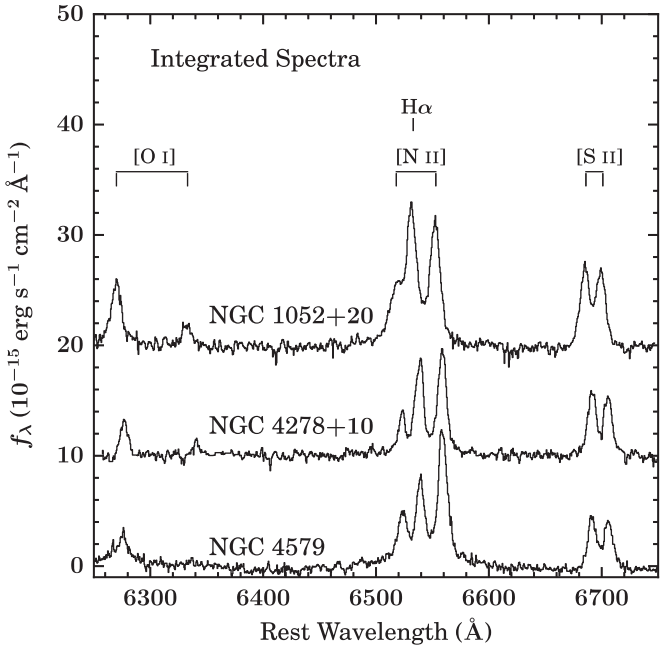

Figure 19. Same as Figure 7, for integrated red spectra, constructed as described in Section 6.1. The broad wings on the Hα line are discernible in NGC 1052 and NGC 4579.

2 for the Mg II $\lambda\lambda$2798, 2803 doublet, and 1/3 for all the others. Finally, if the weaker line in a doublet was not detected or blended with another line, we also constrained the wavelength ratio of the two lines. The strong blends in the Hα complex in both the unresolved nuclear and the central resolved spectra NGC 1052 required us to constrain the [N II] $\lambda\lambda$6548, 6583 widths to equal the [S II] $\lambda\lambda$6716, 6731 widths. In the unresolved nuclear spectrum of NGC 1052, we further constrained the width of narrow Hα to equal that of Hβ. We measured all emission lines detected with at least a 3σ confidence, and measured upper limits for all expected

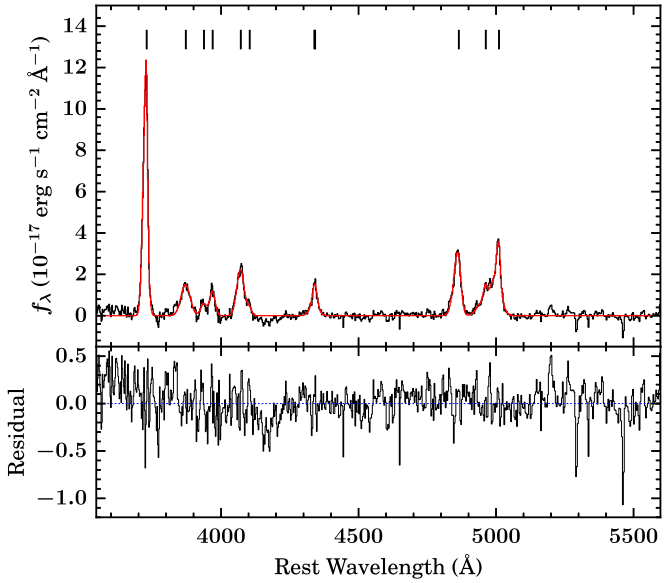

Figure 20. Emission line decomposition for the central blue spectrum of the extended resolved source in NGC 4278. The top panel has the data shown in black and the fit from `specfit` shown in red (smooth, solid line). Each emission line is marked with a vertical hash. The bottom panel shows the residual when the model is subtracted from the data, with a blue dashed line at zero to guide the eye. See Section 6.2 for a discussion on emission line measurements.

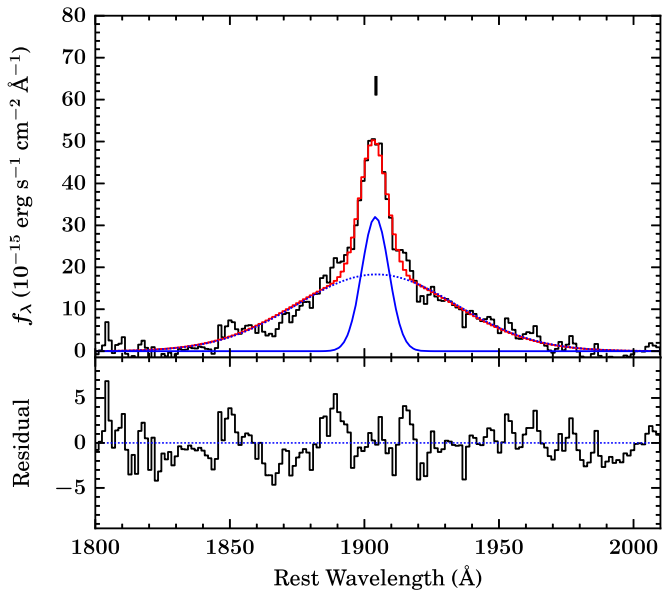

Figure 21. Fit of the broad and narrow C III] λ1909 line components in the spectrum of the spatially unresolved nuclear source of NGC 4579. The top panel has the data shown in black, the total fit from `specfit` shown in red (upper smooth curve) and the emission line components shown in blue. The centroids of the emission line components overlap and are marked with a vertical hash. The dashed blue line shows the broad component, and the solid blue (lower smooth curve) line shows the narrow line component. The bottom panel shows the residual when the model is subtracted from the data, with a blue dashed line at zero to guide the eye.

lines in every spectrum where at least one line was detected. To calculate the upper limits, the shape of [O III] λ5007 from the central resolved spectrum for each object was scaled, except for [Fe X] λ6374 and [Fe XIV] λ5303 for which we used Hβ for the upper limit calculation. The error bars on the line fluxes were calculated by `specfit`, and they correspond to a 1σ confidence interval for one interesting parameter. For

Table 4
Narrow Emission-line Measurements from the NUV Spectra

Galaxy	Dist.[a] (pc)	Emission-Line Flux[b]						
		C III]λ1909	N IIλ2142	C II]λ2326	[O II]λ2470	Mg IIλ2798	Mg IIλ2803	Mg Iλ2852
NGC 1052	−19	<10	<6	5.1 ± 0.6	<5	<8	<8	<9
	−15	<20	<5	12.2 ± 0.8	<5	4.0 ± 0.6	2.0 ± 0.3	<9
	−11	12 ± 2	<10	17.2 ± 0.9	5.0 ± 0.7	8.7 ± 0.8	4.3 ± 0.4	<5
	−6	16 ± 2	<10	27.0 ± 0.9	11 ± 1	20 ± 1	9.8 ± 0.5	<8
	0	9 ± 3	<7	24 ± 1	12 ± 1	17 ± 1	8.6 ± 0.5	<8
	4	9 ± 1	<7	20 ± 10	7.1 ± 0.9	10 ± 10	10 ± 10	<8
	9	<20	<1	13 ± 2	<1	3.8 ± 0.7	1.9 ± 0.4	<9
	13	<20	<9	7 ± 1	<7	6 ± 1	3.2 ± 0.6	<6
	17	5 ± 2	<10	7.1 ± 0.8	<5	2.2 ± 0.7	1.1 ± 0.4	<8
	22	<20	<8	4.7 ± 0.7	<8	<4	<8	<8
	Unres	91 ± 3	<30	130 ± 20	70 ± 10	160 ± 60	80 ± 30	<40
NGC 4278	−13	<20	<10	8.8 ± 0.8	<10	3.8 ± 0.8	1.9 ± 0.4	<10
	−9	<20	<10	15 ± 1	10 ± 10	9 ± 2	5 ± 1	<20
	−5	16 ± 3	<20	38 ± 3	8 ± 1	29 ± 2	14 ± 1	<10
	0	21 ± 3	<30	83 ± 9	23 ± 2	60 ± 3	30 ± 1	<20
	4	<40	<20	46 ± 2	16 ± 2	55 ± 3	27 ± 1	<10
	7	13 ± 5	<20	11 ± 2	<20	18 ± 5	9 ± 3	<20
	11	<20	<10	4.5 ± 0.9	<9	<20	<9	<20
	18	<20	<10	8 ± 1	<10	<20	<9	<20
NGC 4579	Unres	40 ± 1	2.2 ± 0.6	34 ± 3	8 ± 1	34 ± 4	17 ± 2	16 ± 2

Notes.
[a] Distance with respect to nuclear row in 2D spectrum, while "Unres" refers to the unresolved nuclear source spectrum.
[b] Flux is presented in units of 10^{-17} erg s^{-1} cm^{-2}.

all doublets constrained by a fixed flux ratio, the error bar on the weaker line was obtained from the error bar on the stronger line. The measured line fluxes reflect the qualitative trend in the relative intensities discussed in Section 6.1. As an example, we show in Figure 22 the variation of the the [O III] λ5007 and [O II] λ3727 line strengths of NGC 1052 and their ratio. The [O III]/[O II] ratio is higher in the nucleus, and declines to a constant non-zero value at about 20 pc from the nucleus. This suggests a change in the excitation mechanism, as we discuss in Section 8.

6.3. Kinematics of the Line-emitting Gas

To probe the kinematics of the line-emitting gas, we use the centroid velocities and FWHM of selected emission lines. As we noted in Section 2, Walsh et al. (2008) made detailed measurements of these quantities for the three galaxies we study here using the [N II] λ6548 line. They used the same red spectra that we use here, which have a high enough spectral resolution to allow one to study the line profiles. We supplemented those measurements with measurements of the [S II] λλ6716, 6731 and [O I] λ6363 lines, which are not near the end of the spectra and relatively easy to deblend. Our newly acquired blue and NUV spectra have a lower spectral resolution than the red spectra, with the result that the emission lines in these spectra are not as well resolved. Therefore, we measure only the centroid of [O II] λ3727, the strongest line at substantial distances from the nucleus.

The results of our measurements are in good agreement with those of Walsh et al. (2008), therefore we refer the reader to their Figures 2(a), (h), (i), and 4 for a graphical illustration. In summary, while two of the objects show some structure, none of the galaxies have regular disk rotation. NGC 1052 superficially appears to have disk rotation but has evidence of an outflow, NGC 4278 has some rotational structure but a kinematic twist near the center, and NGC 4579 does not have any evidence for regular rotation. The velocity difference between the extrema of the radial velocity curves is 400–600 km s^{-1}. The FWHM of the lines at distances greater than 20 pc from the nucleus of each galaxy is in the range 150–350 km s^{-1}, according to the measurements of Walsh et al. (2008). Our measurements were made after grouping together spectra from adjacent rows, therefore the FWHM of the lines are higher as a result of the velocity gradients, falling in the range 200–500 km s^{-1}. In the inner 20 pc the FWHM of the lines rise steeply, reaching values twice as large as those outside of 20 pc.

6.4. Extinction Corrections

We calculated and applied extinction corrections to the emission line fluxes after they were measured. Since our galaxies have $z < 0.005$, we applied a single correction representing both extinction at the source and extinction in the Milky Way. We calculated A_V assuming the Cardelli law (Cardelli et al. 1989) and $R_V = 3.1$. The observed Hα/Hβ ratio in each galaxy was compared iteratively to an assumed intrinsic ratio which changed based on the dominant excitation mechanism at that physical scale.

We found the appropriate excitation mechanism of the spectrum by comparing reddening insensitive diagnostic line ratios to the models as we describe in Section 8. We applied the correction according to the expected intrinsic ratio and compared the corrected diagnostic line ratios to the same sets of models again. If the difference between the uncorrected and corrected line ratios did not change the inferred dominant excitation mechanism at that physical distance from the nucleus, we adopted that intrinsic ratio. Additional details about the models are deferred to Section 8.

Table 5
Narrow Emission-line Measurements from the NGC 1052 Blue Spectra

Dist.[a]	Emission-Line Flux[b]															
(pc)	[O II] 3727	[Ne III] 3869	H8+He I 3890	[Ne III] 3967	H7+He II 3970	[S II] 4069, 4076	Hδ 4101	Hγ 4341	[O III] 4363	He II 4686	Hβ 4861	[O III] 4959	[O III] 5007	[Fe VII] 5160	[Fe VI] 5177	[N I] 5200	[Fe XIV] 5303
−91	5 ± 7	<8	<8	<3	<8	<6	<6	<3	<3	<4	<10	<2	<6	<3	<3	<3	<5
−82	<20	<6	<9	<2	<4	<5	<4	<4	<4	<5	<6	1.0 ± 0.3	3 ± 1	<3	<3	<5	<6
−73	8 ± 2	<6	<6	<2	<4	<5	<5	<4	<4	<5	<5	1.3 ± 0.3	3.8 ± 0.9	<5	<5	<5	<5
−65	12 ± 2	<8	<8	<3	<8	<7	<7	<4	<4	<4	<5	1.8 ± 0.5	5 ± 2	<4	<4	<3	<5
−56	16 ± 3	<5	<5	<2	<9	<7	<6	<5	<5	<4	<7	<2	<6	<4	<4	2 ± 1	<5
−47	25 ± 2	<10	<10	<4	<7	<8	<4	<4	<4	<7	6 ± 1	2.3 ± 0.4	7 ± 1	<5	<5	<5	<5
−39	26 ± 2	<5	<5	<2	<7	<7	<7	2 ± 1	<6	<4	9 ± 2	2.9 ± 0.4	9 ± 1	<8	<8	<7	<7
−30	39 ± 3	<9	<9	<3	<8	<8	<8	8 ± 1	<6	<5	16 ± 2	4.4 ± 0.6	13 ± 2	5 ± 2	<4	7 ± 6	<6
−22	78 ± 2	4 ± 1	5 ± 5	1.3 ± 0.4	3 ± 1	5 ± 1	<6	10 ± 1	<3	<6	23 ± 2	8.1 ± 0.5	24 ± 1	6 ± 3	<7	10 ± 2	<8
−13	172 ± 3	21 ± 4	4 ± 3	7 ± 1	<9	25 ± 3	<8	32 ± 3	<5	<7	95 ± 4	50.6 ± 0.9	152 ± 3	8 ± 2	<9	17 ± 2	<10
0	212 ± 3	43 ± 2	<8	14.3 ± 0.8	7 ± 7	51 ± 2	14 ± 2	28 ± 4	14 ± 3	8 ± 3	130 ± 30	113 ± 1	340 ± 4	15 ± 5	<10	38 ± 9	<6
9	96 ± 3	23 ± 2	6 ± 4	7.7 ± 0.6	8 ± 2	19 ± 2	6 ± 2	15 ± 5	<6	<5	50 ± 40	54 ± 1	162 ± 4	10 ± 8	<4	30 ± 10	<6
17	138 ± 2	22 ± 2	4 ± 2	7.4 ± 0.7	6 ± 2	19 ± 3	14 ± 3	24 ± 2	<3	<6	40 ± 3	22.4 ± 0.6	67 ± 2	5 ± 2	<6	19 ± 2	<6
26	61 ± 2	6 ± 2	3 ± 2	2.1 ± 0.5	3 ± 2	<8	<8	5.0 ± 0.3	<5	<4	11 ± 2	3.5 ± 0.5	10 ± 2	<7	<7	7 ± 2	<6
34	30 ± 2	4 ± 1	<7	1.4 ± 0.4	<8	<6	4 ± 1	<4	<4	<5	8 ± 2	2.5 ± 0.4	8 ± 1	<7	<7	5 ± 1	<6
43	26.3 ± 0.9	<10	<10	<4	<6	<7	<7	<3	<3	<7	<4	2.3 ± 0.4	7 ± 1	<5	<5	<5	<5
52	16 ± 2	<10	<10	<3	<7	<4	<5	<5	<5	<3	<4	2.8 ± 0.5	8 ± 1	<6	<6	<4	<6
60	11 ± 3	<10	<10	<3	<9	<6	<5	<5	<5	<3	3 ± 1	1.6 ± 0.4	5 ± 1	<5	<5	<4	<3
69	15 ± 2	<7	<7	<2	<9	<5	<7	<5	<5	<5	<6	1.3 ± 0.4	4 ± 1	<5	<5	<5	<5
78	13 ± 2	<8	<8	<3	<7	<5	<4	<4	<4	<5	<5	2.0 ± 0.3	6 ± 1	<4	<4	<4	<4
86	9 ± 9	<8	<8	<3	<7	<5	<4	<4	<4	<5	<5	<2	<5	<4	<4	<4	<4
Unres	1030 ± 20	100 ± 20	290 ± 20	33 ± 6	90 ± 40	810 ± 30	20 ± 70	500 ± 100	400 ± 300	40 ± 20	951 ± 70	1000 ± 60	3000 ± 200	130 ± 10	<40	190 ± 20	<60
Integ	8800 ± 200	1700 ± 300	800 ± 100	560 ± 90	400 ± 300	2000 ± 200	500 ± 200	2000 ± 1000	<600	<600	3900 ± 300	2810 ± 70	8400 ± 200	800 ± 400	<500	1500 ± 300	<700

Notes.
[a] Distance with respect to nuclear row in 2D spectrum, while "Unres" and "Integ" refer to the unresolved nuclear source and integrated spectra, respectively.
[b] Flux is presented in units of 10^{-17} erg s^{-1} cm^{-2}.

Table 6
Narrow Emission-line Measurements from the NGC 4278 Blue Spectra

Dist.[a]	Emission-Line Flux[b]															
(pc)	[O II] 3727	[Ne III] 3869	H8+He I 3890	[Ne III] 3967	H7+He II 3970	[S II] 4069, 4076	Hδ 4101	Hγ 4341	[O III] 4363	He II 4686	Hβ 4861	[O III] 4959	[O III] 5007	[Fe VII] 5160	[Fe VI] 5177	[N I] 5200	[Fe XIV] 5303
−72	20 ± 3	<10	<10	<4	<10	<10	<10	<6	<6	<7	6 ± 2	1.5 ± 0.6	4 ± 2	<8	<8	<6	<4
−65	26 ± 3	<10	<8	<3	<10	<10	<10	<9	<9	<9	5 ± 1	1.8 ± 0.5	6 ± 2	<10	<10	<9	<6
−58	42 ± 2	<10	<10	<4	<10	<10	<10	2.9 ± 0.9	<7	<6	6 ± 1	3.1 ± 0.4	9 ± 1	<6	<6	<6	<4
−51	54 ± 2	3 ± 2	<9	1.1 ± 0.6	<10	<10	<8	4.7 ± 0.9	<6	<7	8 ± 1	3.0 ± 0.4	9 ± 1	<5	<5	6 ± 2	<5
−43	53 ± 5	<20	<20	<6	<20	<10	<10	5 ± 2	<5	<8	11 ± 3	3.5 ± 0.9	10 ± 3	<7	<7	<10	<5
−36	57 ± 3	<20	<20	<5	4 ± 2	<10	<10	4.3 ± 0.8	<10	<7	9 ± 1	4.5 ± 0.7	13 ± 2	<8	<8	7 ± 2	<6
−29	51 ± 5	<10	<10	<4	<8	<10	<9	5 ± 1	<10	<10	11 ± 1	5.4 ± 0.7	16 ± 2	<10	<10	<10	<5
−22	57 ± 2	<20	<20	<5	<10	<10	<10	<10	<10	<9	10 ± 1	4.9 ± 0.6	15 ± 2	<9	<9	<7	<7
−15	78 ± 2	3.2 ± 0.2	<10	1.05 ± 0.06	3 ± 1	6 ± 1	<10	<8	<7	<10	11 ± 1	4.8 ± 0.5	14 ± 2	<8	<8	<7	<5
−7	166 ± 2	9 ± 3	<10	3.2 ± 0.9	4.4 ± 0.5	13 ± 2	<10	8 ± 1	<20	<10	31 ± 2	13.0 ± 0.6	39 ± 2	<10	<10	<10	<10
0	240 ± 20	<10	63 ± 4	<3	30 ± 2	75 ± 3	8 ± 2	40 ± 10	<10	<6	98 ± 10	41 ± 2	124 ± 6	<10	<10	<10	<10
11	85 ± 2	<20	<20	<6	<20	45 ± 3	<10	39 ± 2	<10	<9	35 ± 3	15.1 ± 0.6	45 ± 2	<10	<10	<7	<10
18	80 ± 2	<10	<10	<4	<10	<10	<10	9 ± 2	<10	<8	10 ± 2	6.5 ± 0.5	20 ± 2	<8	<8	<10	<5
25	102 ± 8	<20	<20	<7	<10	<20	<10	9 ± 5	<10	<8	16 ± 6	5 ± 2	16 ± 7	<7	<7	9 ± 7	<7
33	60 ± 10	<10	<10	<5	<10	<20	<20	<8	<8	<8	13 ± 9	4 ± 2	12 ± 7	<10	<10	<10	<4
40	30 ± 20	<10	<10	<4	<8	<7	<7	<20	<20	<10	<7	<2	<6	<10	<10	<10	<6
47	30 ± 20	<20	<20	<5	<9	<10	<10	<10	<10	<8	<5	<2	<5	<6	<6	<6	<4
54	20 ± 10	<20	<20	<6	<10	<10	<10	<10	<10	<9	<10	<3	<8	<8	<8	<8	<4
61	16 ± 2	<20	<20	<5	<20	<10	<10	<10	<10	<8	<10	<4	<10	<9	<9	<9	<5
69	15 ± 2	<10	<10	<4	<10	<9	<9	<10	<10	<9	<2	1.2 ± 0.2	3.5 ± 0.7	<7	<7	<7	<5
76	11 ± 2	<8	<8	<3	<9	<9	<9	<10	<10	<10	<8	<3	<10	<9	<9	<9	<4
Integ	13000 ± 1000	<2000	<2000	<600	<2000	<2000	<2000	<1000	<1000	<1000	2000 ± 1000	1000 ± 400	3000 ± 1000	<2000	<2000	<2000	<1000

Notes.
[a] Distance with respect to nuclear row in 2D spectrum, while "Integ" refers to the integrated spectrum.
[b] Flux is presented in units of 10^{-17} erg s^{-1} cm^{-2}.

Table 7
Narrow Emission-line Measurements from the NGC 4579 Blue Spectra

Dist.[a]	Emission-Line Flux[b]															
(pc)	[O II] 3727	[Ne III] 3869	H8+He I 3890	[Ne III] 3967	H7+He II 3970	[S II] 4069, 4076	Hδ 4101	Hγ 4341	[O III] 4363	He II 4686	Hβ 4861	[O III] 4959	[O III] 5007	[Fe VII] 5160	[Fe VI] 5177	[N I] 5200	[Fe XIV] 5303
−85	5 ± 1	<6	<6	<2	<4	<4	<4	<3	<3	<3	<4	<1	<4	<4	<4	<2	<4
−77	4 ± 1	<4	<4	<1	<5	<4	<4	<4	<4	<2	<4	<1	<4	<3	<3	<2	<4
−69	9 ± 1	<6	<6	<2	<6	<3	<5	<3	<3	<4	<3	<1	<3	<4	<4	<3	<4
−61	<6	5 ± 2	<4	1.5 ± 0.5	<5	<4	<5	<1	<1	<3	<3	0.9 ± 0.3	3 ± 1	<5	<5	<4	<6
−53	13 ± 1	<5	<5	<2	<5	<6	<4	<4	<4	<4	<5	2.1 ± 0.3	6 ± 1	<2	<2	<2	<5
−45	12 ± 1	<5	<5	<2	<7	<3	<4	<2	<2	<4	6 ± 2	2.5 ± 0.4	8 ± 1	<3	<3	<3	<4
−37	10 ± 1	<6	<5	<2	<7	<6	<5	<5	<5	<4	<5	5.2 ± 0.6	16 ± 2	<4	<4	<3	<5
−28	23 ± 2	<6	<6	<2	<6	<3	<4	<3	<3	<4	<6	7.6 ± 0.5	23 ± 2	<5	<5	<6	<6
−20	42 ± 2	<5	<5	<2	<5	<7	<4	9 ± 2	<4	<3	15 ± 7	10.0 ± 0.5	30 ± 2	<6	<6	<6	<7
−12	120 ± 20	55 ± 4	<10	18 ± 1	11 ± 5	50 ± 10	<6	113 ± 5	<5	<8	60 ± 10	63 ± 2	188 ± 5	10 ± 3	<8	25 ± 3	<10
0	510 ± 70	390 ± 10	<60	129 ± 4	70 ± 20	218 ± 9	96 ± 6	260 ± 20	<30	<20	320 ± 30	248 ± 3	744 ± 8	90 ± 10	<10	60 ± 10	<20
8	260 ± 30	169 ± 8	<20	56 ± 3	19 ± 8	90 ± 20	<20	<100	<100	<10	130 ± 30	113 ± 4	340 ± 10	<20	<20	<20	<20
16	62 ± 3	<7	<7	<2	<7	<6	<6	<4	<4	<4	19 ± 5	19.5 ± 0.9	58 ± 3	<7	<7	<7	<9
24	40 ± 2	<4	<4	<1	<7	<6	<5	<4	<4	<4	<7	9 ± 1	29 ± 3	<6	<6	<6	<9
33	41 ± 1	<6	<6	<2	<3	<5	<4	<4	<4	<6	5 ± 3	5.4 ± 0.5	16 ± 2	<5	<5	<5	<5
41	35 ± 1	<5	<5	<2	<7	<5	<5	<4	<4	<5	7 ± 3	5.1 ± 0.5	15 ± 2	<5	<5	<5	<6
49	31 ± 1	<5	<5	<2	<5	<5	<5	<5	<5	<3	8 ± 1	4.6 ± 0.5	14 ± 2	<4	<4	<4	<5
57	29 ± 2	<5	<5	<2	<5	<5	<6	7 ± 1	<5	<4	12 ± 2	4.4 ± 0.4	13 ± 1	<5	<5	<5	<6
65	24 ± 2	<6	<6	<2	<6	<5	<5	<6	<6	<2	12 ± 4	4.1 ± 0.4	12 ± 1	<5	<5	<5	<5
73	21 ± 1	<4	<4	<1	<4	<4	<4	<6	<6	<4	8 ± 2	2.1 ± 0.3	6.4 ± 0.9	<3	<3	<3	<4
81	16 ± 1	<4	<4	<1	<3	<4	<4	<4	<4	<4	6 ± 2	1.6 ± 0.3	5 ± 1	<3	<3	<3	<6
Unres	981 ± 90	800 ± 200	600 ± 100	270 ± 60	230 ± 90	690 ± 90	<40	971 ± 50	<40	<60	430 ± 20	680 ± 10	2050 ± 40	120 ± 50	<70	200 ± 200	<90
Integ	7100 ± 200	2700 ± 300	<700	910 ± 90	400 ± 200	1200 ± 200	<500	2100 ± 300	<500	<500	3100 ± 300	2200 ± 100	6600 ± 300	500 ± 300	<300	900 ± 200	<300

Notes.
[a] Distance with respect to nuclear row in 2D spectrum, while "Unres" and "Integ" refer to the unresolved nuclear source and integrated spectra, respectively.
[b] Flux is presented in units of 10^{-17} erg s^{-1} cm^{-2}.

Table 8
Narrow Emission-line Measurements from the Red Spectra

Galaxy	Dist.[a] (pc)	Emission-Line Flux[b]							
		[O I]λ6300	[O I]λ6363	[Fe X]λ6374	[N II]λ6548	Hαλ6563	[N II]λ6583	[S II]λ6716	[S II]λ6731
NGC 1052	−91	6.4 ± 0.9	2.1 ± 0.3	<10	1.8 ± 0.2	8 ± 1	5.4 ± 0.7	5.3 ± 0.6	3.5 ± 0.6
	−82	<9	<3	<9	3.5 ± 0.2	12.9 ± 0.9	10.5 ± 0.7	5.4 ± 0.6	5.1 ± 0.6
	−73	<10	<5	<10	3.6 ± 0.3	12 ± 1	11 ± 1	6.5 ± 0.8	3.0 ± 0.6
	−65	2.9 ± 0.6	1.0 ± 0.2	<7	3.7 ± 0.4	11 ± 2	11 ± 1	7 ± 1	3.8 ± 0.7
	−56	5 ± 1	1.6 ± 0.3	<10	6.1 ± 0.6	20 ± 2	18 ± 2	7.7 ± 0.8	6.3 ± 0.8
	−47	<10	<4	<20	6.5 ± 0.4	18 ± 2	20 ± 1	14 ± 1	9 ± 1
	−39	11 ± 1	3.7 ± 0.4	<10	9.7 ± 0.6	29 ± 2	29 ± 2	20 ± 1	16 ± 1
	−30	18 ± 2	5.9 ± 0.6	<10	16 ± 2	57 ± 3	47 ± 6	32 ± 1	29 ± 1
	−22	31 ± 2	10.2 ± 0.5	<20	34 ± 8	119 ± 5	100 ± 20	70 ± 2	61 ± 2
	−13	230 ± 20	78 ± 8	<20	76 ± 3	600 ± 30	230 ± 10	190 ± 50	170 ± 30
	0	560 ± 40	190 ± 10	<40	200 ± 60	1460 ± 80	600 ± 200	180 ± 10	290 ± 20
	9	149 ± 5	50 ± 2	<20	113 ± 4	430 ± 30	340 ± 10	160 ± 20	210 ± 40
	17	56 ± 2	18.6 ± 0.8	<10	51 ± 2	128 ± 4	152 ± 5	116 ± 5	109 ± 5
	26	24 ± 1	7.9 ± 0.4	<20	25.7 ± 0.6	69 ± 2	77 ± 2	55 ± 2	52 ± 1
	34	10.1 ± 0.9	3.4 ± 0.3	<10	10.6 ± 0.3	31 ± 1	31.9 ± 0.9	22.3 ± 0.8	19.1 ± 0.8
	43	8 ± 1	2.6 ± 0.3	<10	5.1 ± 0.4	18 ± 1	15 ± 1	14 ± 1	11 ± 1
	52	6 ± 1	2.1 ± 0.5	<20	4.9 ± 0.4	14 ± 2	15 ± 1	10 ± 1	7 ± 1
	60	2 ± 1	0.7 ± 0.4	<10	4.0 ± 0.6	13 ± 3	12 ± 2	7 ± 2	6 ± 2
	69	3.0 ± 0.8	1.0 ± 0.3	<10	3.5 ± 0.3	12 ± 1	10.4 ± 0.9	7.5 ± 0.8	5.2 ± 0.7
	78	<20	<5	<20	3.3 ± 0.2	11.1 ± 0.8	9.8 ± 0.6	8.0 ± 0.5	7.2 ± 0.6
	86	<10	<3	<10	3.2 ± 0.3	7.6 ± 0.6	9.7 ± 0.8	7.8 ± 0.8	4.7 ± 0.7
	Unres	2700 ± 400	900 ± 100	<100	400 ± 100	3500 ± 500	1200 ± 300	500 ± 400	2200 ± 800
	Integ	6000 ± 1000	2100 ± 400	<1000	4600 ± 400	16000 ± 2000	14000 ± 1000	7000 ± 1000	7000 ± 1000
NGC 4278	−72	<9	<3	<9	3.5 ± 0.3	7.6 ± 0.8	10.4 ± 0.8	6.9 ± 0.8	6.1 ± 0.7
	−65	3 ± 2	0.8 ± 0.6	<10	4.8 ± 0.8	9 ± 2	14 ± 2	8 ± 2	9 ± 2
	−58	5 ± 1	1.7 ± 0.3	<10	8.3 ± 0.4	21 ± 1	25 ± 1	16 ± 1	13.0 ± 0.9
	−51	13 ± 1	4.3 ± 0.3	<10	8.8 ± 0.3	26.9 ± 0.8	26 ± 1	23 ± 1	18 ± 1
	−43	13.4 ± 0.8	4.5 ± 0.3	<10	14.7 ± 0.3	37.6 ± 0.9	44.1 ± 0.9	29.7 ± 0.8	23.3 ± 0.7
	−36	15.3 ± 0.9	5.1 ± 0.3	<9	17 ± 2	41 ± 1	51 ± 7	33 ± 1	28.4 ± 0.9
	−29	12 ± 2	4.0 ± 0.5	<20	12 ± 2	37 ± 2	35 ± 7	26 ± 2	23 ± 2
	−22	10.0 ± 0.7	3.3 ± 0.2	<10	12.5 ± 0.3	35 ± 1	37 ± 1	19.8 ± 0.7	18.0 ± 0.7
	−15	12 ± 1	3.9 ± 0.4	<10	17 ± 2	47 ± 2	50 ± 6	22 ± 1	24 ± 1
	−7	25 ± 2	8.2 ± 0.6	<10	24 ± 6	41 ± 2	70 ± 20	36 ± 2	40 ± 2
	0	40 ± 10	13 ± 4	<20	70 ± 30	400 ± 100	220 ± 90	70 ± 40	90 ± 40
	11	32 ± 6	11 ± 2	<20	12 ± 2	270 ± 10	35 ± 5	32 ± 3	30 ± 3
	18	18 ± 1	6.1 ± 0.4	<10	21 ± 1	50 ± 2	62 ± 3	29 ± 5	31 ± 4
	25	26 ± 1	8.7 ± 0.5	<10	26 ± 1	81 ± 9	78 ± 4	49 ± 3	44 ± 2
	33	19.7 ± 0.8	6.6 ± 0.3	<10	20.1 ± 0.4	50 ± 1	60 ± 1	34.6 ± 0.9	32.4 ± 0.8
	40	11.1 ± 0.8	3.7 ± 0.3	<30	8.9 ± 0.3	25 ± 1	26.6 ± 0.9	17.3 ± 0.8	16.4 ± 0.8
	47	4 ± 2	1.3 ± 0.8	<10	6 ± 4	15 ± 4	20 ± 10	14 ± 4	11 ± 4
	54	2 ± 1	0.5 ± 0.4	<10	5 ± 1	14 ± 3	14 ± 4	9 ± 3	9 ± 3
	61	3.7 ± 0.7	1.2 ± 0.2	<30	4.5 ± 0.4	12 ± 1	13 ± 1	8.0 ± 0.8	6.8 ± 0.8
	69	3 ± 4	1 ± 1	<10	3 ± 1	9 ± 4	10 ± 4	7 ± 4	6 ± 4
	76	<20	<8	<20	1.7 ± 0.5	9 ± 2	5 ± 2	5 ± 2	4 ± 2
	Integ	2500 ± 200	820 ± 70	<3000	3400 ± 100	8900 ± 300	10100 ± 300	5600 ± 200	5100 ± 200
NGC 4579	−85	<10	<4	<10	2.4 ± 0.5	4 ± 2	7 ± 1	<7	<7
	−77	<9	<3	<9	3 ± 20	4 ± 14	10 ± 50	<14	<14
	−69	<9	<3	<9	4.0 ± 0.7	4 ± 2	12 ± 2	<6	<6
	−61	<10	<3	<10	4.7 ± 0.3	11 ± 1	14 ± 1	3.8 ± 0.6	3.4 ± 0.6
	−53	<9	<3	<9	6.0 ± 0.4	14 ± 1	18 ± 1	9.9 ± 0.9	5.5 ± 0.8
	−45	<20	<5	<9	8.3 ± 0.4	13.6 ± 0.9	25 ± 1	4.9 ± 0.7	5.1 ± 0.7
	−37	<10	<4	<10	8.8 ± 0.5	6 ± 2	26 ± 1	12 ± 1	7.6 ± 0.9
	−28	6 ± 1	2.2 ± 0.4	<10	11.6 ± 0.5	29 ± 2	35 ± 2	13.1 ± 0.8	12.4 ± 0.9
	−20	14 ± 3	4.7 ± 0.9	<20	18 ± 2	60 ± 10	54 ± 7	29 ± 1	31 ± 1
	−12	39 ± 2	12.9 ± 0.6	<10	39 ± 1	<20	118 ± 4	52 ± 2	47 ± 2
	0[c]	...	...	...	...	...	...	...	...
	8[c]	...	...	...	...	...	...	...	...
	16	16 ± 7	5 ± 2	<20	11 ± 2	<10	34 ± 6	14 ± 1	25 ± 2
	24	<10	<4	<10	8 ± 4	22 ± 4	20 ± 10	12 ± 3	17 ± 4
	33	14 ± 2	4.6 ± 0.5	<10	9.6 ± 0.6	25 ± 4	29 ± 2	16.5 ± 0.9	19 ± 1
	41	<9	<3	<9	16.6 ± 0.3	27 ± 1	49.7 ± 0.9	18.1 ± 0.7	16.7 ± 0.7
	49	<10	<4	<10	15.9 ± 0.4	28 ± 1	48 ± 1	19 ± 1	14 ± 1
	57	10 ± 1	3.4 ± 0.4	<10	15.2 ± 0.4	35 ± 1	46 ± 1	18 ± 1	14.9 ± 0.9

Table 8
(Continued)

Galaxy	Dist.[a] (pc)	Emission-Line Flux[b]							
		[O I]λ6300	[O I]λ6363	[Fe X]λ6374	[N II]λ6548	Hαλ6563	[N II]λ6583	[S II]λ6716	[S II]λ6731
	65	<10	<4	<10	11.7 ± 0.3	37 ± 1	35 ± 1	16 ± 1	16 ± 1
	73	<10	<4	<10	9.2 ± 0.3	24.1 ± 0.9	27.7 ± 0.8	9.8 ± 0.8	8.8 ± 0.7
	81	<10	<3	<10	7.0 ± 0.4	18 ± 1	21 ± 1	9 ± 1	8 ± 1
	Unres	1100 ± 30	370 ± 10	<100	1100 ± 70	3500 ± 200	3300 ± 200	540 ± 20	530 ± 20
	Integ	3000 ± 1000	1100 ± 400	<1000	3300 ± 700	4000 ± 2000	9900 ± 2000	4100 ± 900	4100 ± 900

Notes.
[a] Distance with respect to nuclear row in 2D spectrum, while "Unres" and "Integ" refer to the unresolved nuclear source and integrated spectra, respectively.
[b] Flux is presented in units of 10^{-17} erg s^{-1} cm^{-2}.
[c] We were not able to measure the line strengths in the resolved emission near the nucleus due to the overwhelming strength of the unresolved nuclear source. See Section 4.1 for details.

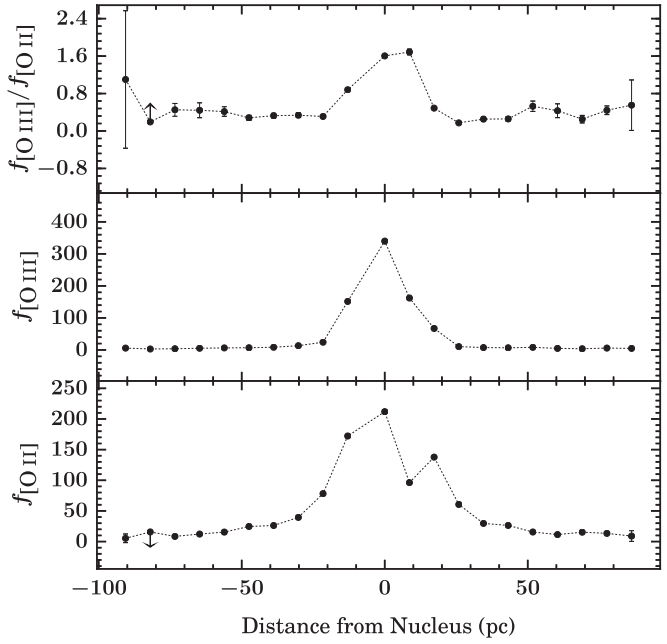

Figure 22. Change of the [O III] λ5007 and [O II] λ3727 emission line fluxes in NGC 1052 with distance from the nucleus (see Section 6.2). The flux scale on the vertical axis is in units of 10^{-18} erg s^{-1} cm^{-2} Å^{-1} arcsec^{-2}. Top: measured line ratio of [O III]/[O II]. The line ratio changes and flattens out to a non-zero value at 20 pc from the nucleus, suggesting a change in the excitation mechanism. Middle: change in the measured line flux of [O III] λ5007. Bottom: change in the measured line flux of [O II] λ3727.

The calculated values of A_V and the assumed intrinsic Hα/Hβ ratios for each spectrum are in Tables 9–11, with the exception of the central spectra of NGC 4579, where the unresolved source overwhelms the resolved emission and makes measurements of the latter impossible. These extinction correction values were also adapted for use in the NUV emission lines, which are probed on a different spatial scale than the extinction measurements. The observed extinction is patchy, and there is no overall trend with distance from the nucleus, which may cause additional uncertainty in the NUV emission line ratios discussed in Section 8.3.

We note that since the extinction corrections are derived from the ratio of two lines observed with different gratings, they are affected by the uncertainties in spatial decomposition discussed in Section 4.2. However, we emphasize that (a) uncertainties in spatial decomposition affect only extinction estimates for spectra extracted from ±3 pixel rows from the nucleus, and (b) uncertainties in extinction affect critically only one of the optical diagnostic line ratios that we use in later sections, the [O III] λ5007/[O II] λ3727 ratio. All other optical line ratios that we use involve closely separated lines and thus are insensitive to extinction corrections. The NUV line ratios are also affected but these are not crucial to our overall conclusions. We use reddening arrows to indicate the effects of extinction uncertainties in the diagnostic line ratio diagrams we present in later sections.

Table 9
NGC 1052 A_V Values and Intrinsic Hα/Hβ Ratios

Distance (pc)[a]	A_V	$[H\alpha/H\beta]_{int}$[b]	Mechanism
−91	0.000	3.01	Shock
−82	0.000	3.01	Shock
−73	0.000	3.01	Shock
−65	0.000	3.01	Shock
−56	0.000	3.01	Shock
−47	0.122	3.01	Shock
−39	0.000	3.01	Shock
−30	0.479	3.01	Shock
−22	1.700	3.01	Shock
−13	2.253	3.10	AGN–NLR
0	4.025	3.10	AGN–NLR
+09	3.034	3.10	AGN–NLR
+17	0.177	3.01	Shock
+26	0.958	3.01	Shock
+35	0.887	3.01	Shock
+43	0.000	3.01	Shock
+52	0.000	3.01	Shock
+60	0.190	3.01	Shock
+69	0.000	3.01	Shock
+78	0.000	3.01	Shock
+86	0.000	3.01	Shock
Unresolved	0.575	3.10	AGN–NLR

Notes.
[a] Distance with respect to nuclear row in 2D spectrum.
[b] The adopted intrinsic value of the Hα/Hβ ratio. The value for an AGN–NLR (narrow line region) is from Osterbrock & Ferland (2006, chapter 11). The value for shocks is an average value from the Allen et al. (2008) shock models.

7. Temperature and Density Estimates

We determined the electron temperature and density as a function of distance from the center of each galaxy using the [O III] λ5007/[O III] λ4363 and [S II] λ6716/[S II] λ6731 line

Table 10
NGC 4278 A_V Values and Intrinsic $H\alpha/H\beta$ Ratios

Distance (pc)[a]	A_V	$[H\alpha/H\beta]_{int}$[b]	Mechanism
−72	0.000	3.01	Shock
−65	0.310	3.01	Shock
−58	0.159	3.01	Shock
−51	0.209	3.01	Shock
−43	0.359	3.01	Shock
−36	1.463	3.01	Shock
−29	0.012	3.01	Shock
−22	0.378	3.01	Shock
−15	1.192	3.01	Shock
−07	1.111	3.01	Shock
00	0.807	3.01	Shock
+11	3.009	3.01	Shock
+18	1.502	3.01	Shock
+25	1.587	3.01	Shock
+33	1.496	3.01	Shock
+40	0.000	3.01	Shock
+47	0.329	3.01	Shock
+54	0.000	3.01	Shock
+61	0.000	3.01	Shock
+69	0.000	3.01	Shock
+76	0.000	3.01	Shock

Notes.
[a] Distance with respect to nuclear row in 2D spectrum.
[b] The adopted intrinsic value of the $H\alpha/H\beta$ ratio. This is an average value from the Allen et al. (2008) shock models.

Table 11
NGC 4579 A_V Values and Intrinsic $H\alpha/H\beta$ Ratios

Distance (pc)[a]	A_V	$[H\alpha/H\beta]_{int}$[b]	Mechanism
−85	0.000	2.86	H II
−77	0.000	2.86	H II
−69	0.000	2.86	H II
−61	0.000	2.86	H II
−53	0.000	2.86	H II
−45	0.000	2.86	H II
−37	0.000	2.86	H II
−28	0.000	2.86	H II
−20	0.993	2.86	H II
−12	0.000	3.10	AGN–NLR
00	0.000	3.10	AGN–NLR
+08	0.000	3.10	AGN–NLR
+16	0.000	3.10	AGN–NLR
+24	0.000	2.86	H II
+33	1.749	2.86	H II
+41	1.018	2.86	H II
+49	0.596	2.86	H II
+57	0.024	2.86	H II
+65	0.209	2.86	H II
+73	0.256	2.86	H II
+81	0.073	2.86	H II
Unresolved	3.012	3.10	AGN–NLR

Notes.
[a] Distance with respect to nuclear row in 2D spectrum.
[b] The adopted intrinsic value of the $H\alpha/H\beta$ ratio. The value for an AGN–NLR is from Osterbrock & Ferland (2006, chapter 11). The value for H II is the theoretical value for Case B recombination (Osterbrock 1989).

ratios, respectively, at all distances (e.g., Osterbrock & Ferland 2006, Chapter 5). The temperatures predicted by AGN photoionization models ($T \approx 1$–2×10^4 K; Groves et al. 2004) and from shock models ($T \approx 4 \times 10^4$–1×10^6 K; Allen et al. 2008), both of which are described in more detail in Section 8.2, are sufficiently different to make this a useful diagnostic in principle. The [S II] λ6716/[S II] λ6731 density estimate is useful for comparing our measurements to those of Walsh et al. (2008), as well as for estimating the ionization parameter U in NGC 4278 and NGC 4579 (see the discussion in Section 8.3). Near the nucleus of each galaxy we also detected the [S II] $\lambda\lambda$4069, 4076 and [O II] λ2470 lines, implying a density of $n_e \gtrsim 10^4$ cm^{-3}, which is above the sensitivity threshold of the [S II] $\lambda\lambda$6716, 6731 doublet. We also used these lines to obtain an estimate on the density near the nucleus for all three objects.

The electron temperature is only estimated when the [O III] λ4363 emission line was detected or when the lower limit of [O III] λ5007/[O III] λ4363 > 5, as a limit below that threshold is not useful. The temperature derived for the nucleus of NGC 1052 is $T \approx 4 \times 10^4$ K, which can be explained by shock heating, and meaningful upper limits of $T < 3 \times 10^4$ K are obtained within the central 40 pc. NGC 4278 has very weak [O III] λ4363 emission, and only one meaningful upper limit on the temperature of $T < 3.5 \times 10^4$ K was obtained. For NGC 4579 we were able to obtain limits within the central 20 pc of order $T < 4 \times 10^4$. All of these temperature upper limits are too high to disfavor shock heating, and thus cannot be used to discriminate between the two model families in practice.

We detected the [S II] $\lambda\lambda$6716, 6731 doublet in all objects, and we were able to determine electron densities as a function of distance from the nucleus for all objects. We plot these in Figure 23. The only exceptions are the central two rows in NGC 4579, where no lines were detected (see Section 6), so we do not report density estimates at those distances. Our measured electron densities are consistent with those in Walsh et al. (2008). The high density that was originally seen in the nucleus of NGC 1052 by Walsh et al. was found both in the resolved center of the galaxy and in the unresolved nuclear emission. We also detected the [S II] $\lambda\lambda$4069, 4076 and [O II] λ2470 lines near the nucleus of each galaxy. By combining the temperature estimates obtained from the [O III] diagnostic and the de-reddened [O II] λ2470/[O II] λ3727 and [S II] $\lambda\lambda$4069, 4076/[S II] $\lambda\lambda$6716, 6731 line ratios, we obtained an estimate of the density using the program PyNeb (Luridiana et al. 2015).

The density estimates from both the [S II] and [O II] diagnostics for NGC 4579 and NGC 4278 agree with those obtained via the [S II] $\lambda\lambda$6716, 6731 doublet. The high density seen in the resolved center of NGC 1052 is consistent with $n_e \sim 2 - 6 \times 10^4$ cm^{-3} using both the [S II] and [O II] diagnostics, while the unresolved nuclear source requires an even higher density ($n_e \sim 10^5$ cm^{-3}) to explain the [O II] line ratio. This difference in densities is consistent with the need for a multi-component density model, as described by Dopita et al. (2015) and Gabel et al. (2000).

Even though the nuclear density of NGC 1052 is extremely high, the density estimate from the integrated emission for all three galaxies is of order 10^3 cm^{-3}. This difference in densities highlights the potential of obtaining misleading density estimates from spectra that sample gas with a wide range of physical conditions.

We will use the densities obtained from the spatially resolved spectra to constrain the models and we will also

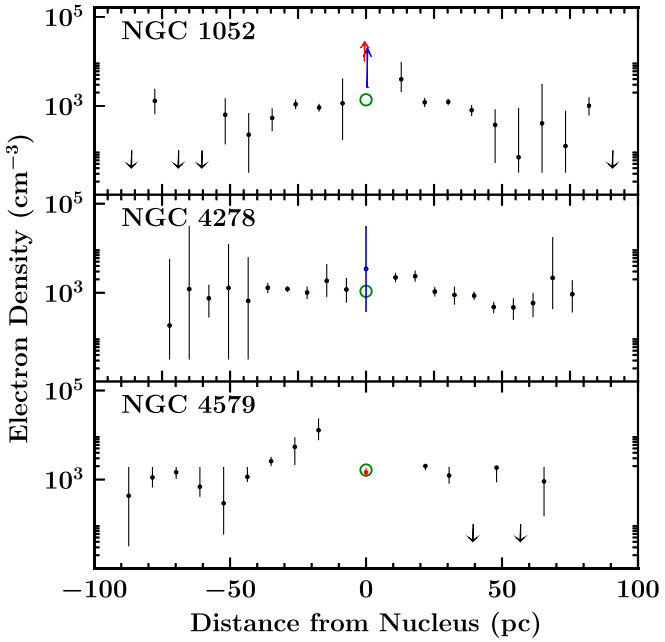

Figure 23. Density estimates from the [S II] $\lambda\lambda$6716, 6731 ratio for all three objects as a function of distance from the nucleus. Red points (at 0 pc) represent the estimate from the spectrum of the spatially unresolved nuclear source for NGC 1052 and NGC 4579, blue points represent the center of the extended, resolved source (at 0 pc, above the unfilled circle in NGC 1052 and NGC 4278), and the green unfilled circles represent the integrated spectrum. The details of the calculation are given in Section 7. The [S II] $\lambda\lambda$6716, 6731 doublet at 0 pc and 8 pc in the extended, resolved source of NGC 4579 are not detected as described in Section 6, so no density estimate is given. The high density found in Walsh et al. (2008) in NGC 1052 is also found here both in the center of the resolved source and the unresolved nuclear source, and is above the sensitivity of this line ratio. The estimates of the nuclear densities for all three objects are discussed in Section 7.

incorporate them into a calculation of the ionization parameter, as described in Section 8.3.

8. Comparison of Emission Line Measurements with Models

8.1. Emission Line Diagnostic Diagrams

In order to diagnose the excitation mechanism of the emission line gas, we used the emission line intensities measured above to form extinction-corrected line ratios, which we plotted in diagnostic diagrams in the spirit of Baldwin et al. (1981, also known as BPT diagrams). We produced four diagnostic diagrams involving optical lines for each galaxy. We also produced three diagnostic diagrams involving NUV lines for NGC 1052 and NGC 4278. In NGC 4579 we only detected an unresolved source in the NUV band hence we did not construct the corresponding diagnostic diagrams. The diagrams, shown in Figures 24–41, are used to assess the mechanisms that excite the gas, whether excitation by fast and slow shocks, or photoionization by an AGN, pAGB stars, or young, massive stars (as in H II regions). We plot the same data in each quadrant of the same figure but superpose a different model grid.

We also compared the upper limits of [Fe X] λ6374/Hβ and [Fe XIV] λ5303/Hβ to shock models from Wilson & Raymond (1999). The highly ionized Fe lines were never detected, so we only have upper limits to these ratios when we detect Hβ. Additionally, we compared the [Ne III] λ3869/[O II] λ3727 to photoionization models for radiatively inefficient accretion flows (RIAFs) from Nagao et al. (2002)[10] for all three galaxies, and we calculated the ionization parameter, U (defined in Section 8.3), as a function of distance for NGC 4278 and NGC 4579. All comparisons to models and the calculated U values are discussed in Section 8.3.

As noted above, four of the seven diagnostic diagrams use optical line ratios: [O III]/Hβ versus [O III]/[O II], [N II]/Hα, [S II]/Hα, and [O I]/Hα (these are commonly used diagrams; e.g., Veilleux & Osterbrock 1987; Kauffmann et al. 2003; Kewley et al. 2006; Ho 2008), and the other three use NUV line ratios: C III]/C II] versus [O II]/C II], [N II]/C II], and Mg II/C II]. The NUV diagrams were chosen according to both the emission lines we were able to measure and the extent of the region that the models occupy in parameter space near the measured values. C III] λ1909 and C II] λ2326 are the only two lines in the NUV spectra that we could consistently measure.

In diagnostic diagrams where at least one line ratio is sensitive to extinction (i.e., the diagram involving [O III]/[O II] and any NUV ratios), we plot reddening arrows. These show how a point in the diagram would move if $E(B-V)$ increased by 1 mag. We note an additional source of uncertainty for the NUV lines. The measured extinction is sampled according to the angular resolution of the blue and red spectra since it comes from the Hα/Hβ ratio, but the NUV line ratios are sampled at a higher angular resolution, requiring us to interpolate the extinction values.

We begin by describing below how the observed line ratios are distributed in the diagnostic diagrams, we review the models in some detail in Section 8.2, and we compare the models to the observations for each individual galaxy in Section 8.3.

NGC 1052. Figure 25 most clearly shows the spatial variation of the [O III]/Hβ ratio. Hβ becomes stronger relative to [O III] λ5007 with increasing distance from the nucleus. The spectrum of the spatially unresolved nuclear source has the largest measured [O III]/Hβ ratio, while the line ratio from the integrated spectrum falls in between that and the off-nuclear resolved spectra. Figure 24 shows a similar trend for the [O III]/[O II] ratio, which decreases with distance from the nucleus. In this case we see a clear separation in the line ratios of the unresolved nuclear source and the off-nuclear resolved emission, with the line ratio from the integrated spectrum and the nuclear spectrum of the resolved source falling between them. The [N II]/Hα and [S II]/Hα ratios are both $\approx$1, for the off-nuclear resolved spectra as shown in Figures 25 and 26, while the unresolved and resolved nuclear emission have ratios $<$1. The [S II]/Hα ratio for the resolved nuclear emission is significantly smaller than 1, and separates itself from the rest of the measurements. The [O I]/Hα ratio in the spatially unresolved nuclear source is $\approx$1, while generally this ratio decreases with distance from the nucleus in the extended emission (see Figure 27). The ratio from the integrated spectrum is similar to those obtained close to the nucleus.

The NUV line ratios have significantly more scatter than the optical ones. There is no apparent trend in the C III]/C II] ratio (Figures 28–30). Generally, the [O II]/C II] ratio in the unresolved source is different from that of resolved

[10] These models employ a harder spectrum of ionizing photons than the standard AGN models.

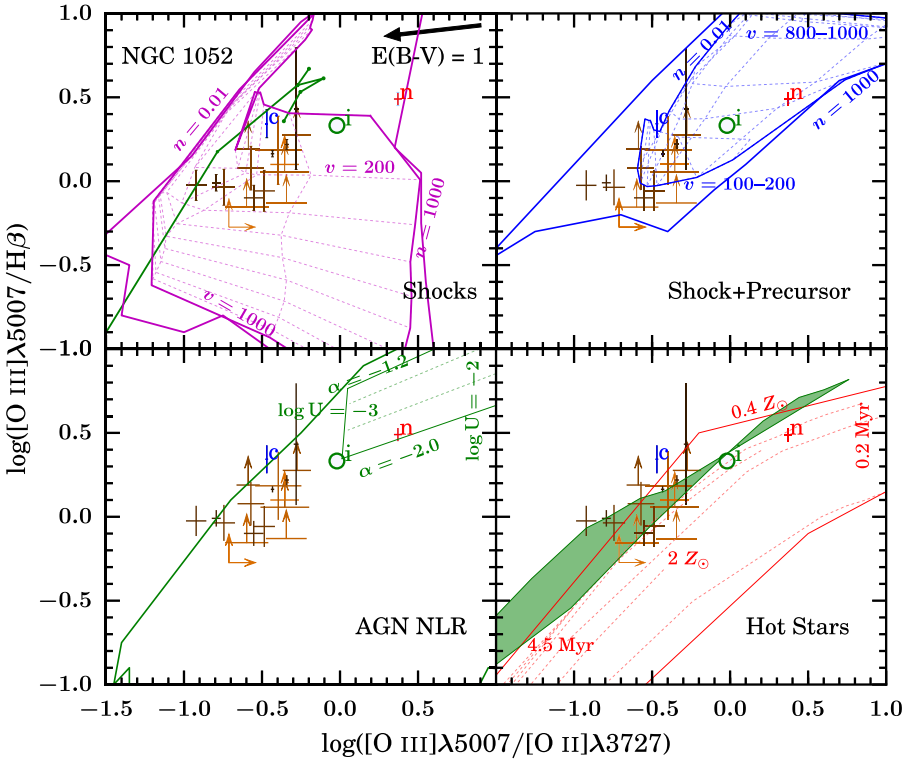

Figure 24. Diagnostic diagram of [O III]/Hβ vs. [O III]/[O II] for NGC 1052. The measurements made along the slit throughout the extended, resolved source are shown in shades of orange (without labels). The darkest orange represents the measurement closest to the nucleus. The blue point labeled "c" represents the center of the resolved source, the red point labeled "n" represents the central, unresolved source, and the unfilled green circle labeled "i" represents the ratios in the integrated spectrum. Limits are indicated with arrows. All models, shown with solid and dotted lines, are described in Section 8.2. Top left: comparison of data to simple shock models (without a precursor). The points connected by the solid green line represent the slow shock models of Shull & McKee (1979), while the purple grid and outline are fast shock models of Allen et al. (2008). The solid black arrow shows the change in the line ratios when an extinction correction of $E(B-V) = 1$ mag is applied. The labels show how density (in cm^{-3}) and velocity (in km s^{-1}) change across the detailed grid. Top right: comparison of data to shock plus precursor models from Allen et al. (2008). The labels show how density (in cm^{-3}) and velocity (in km s^{-1}) change across the detailed grid. Bottom left: comparison of data to AGN NLR photoionization models from Groves et al. (2004), with the labels showing how the ionization parameter and the power-law index of the ionizing continuum change across the detailed grid. Bottom right: comparison of data to H II region models from Dopita et al. (2006). The model tracks are in red and the labels show how age and metallicity change across the grid. The green shaded region represents pAGB star models from Binette et al. (1994).

emission (Figure 28). All of the [N II]/C II] ratios in the resolved emission are upper limits (Figure 29). Finally, the Mg II/C II] ratio in the unresolved nuclear source is higher than what is observed in the resolved emission (Figure 30), the large uncertainties notwithstanding.

NGC 4278. The [O III]/[O II] and [O III]/Hβ ratios do not change systematically with distance from the nucleus, as seen in Figure 31. The [N II]/Hα, [S II]/Hα and [O I]/Hα ratios in the nuclear spectrum are systematically different from those of the resolved, extended emission (see Figures 32–34). All the optical line ratios of the integrated emission are similar to the corresponding ratios observed in the extended, resolved emission (Figures 31–34).

The NUV line ratios do not show any systematic trends as a function of distance from the nucleus. The C III]/C II] and Mg II/C II] line ratios are clustered tightly (Figure 37) while most of the [O II]/C II] and all of the [N II]/C II] ratios in the resolved emission are upper limits (Figures 35, 36).

NGC 4579. Because of the overwhelming strength of the spatially unresolved nuclear source in the red spectrum, we can only measure the [N II]/Hα, [S II]/Hα and [O I]/Hα ratios from the resolved emission starting at 12 pc from the nucleus. The [O III]/Hβ ratio of the resolved emission is similar to that measured in the unresolved nuclear source. As a result, the point representing the unresolved nuclear source is within the cluster of points representing the extended emission in most of the diagnostic diagrams. The [O III]/Hβ versus [S II]/Hα diagram is an exception; in this diagram the point representing the unresolved nuclear source is well separated from the cluster of points representing the extended emission.

The NUV diagnostic diagrams are not plotted because the NUV spectrum of NGC 4579 is dominated by emission from the unresolved AGN.

8.2. Emission Line Models for Different Excitation Mechanisms

As shown in Figures 24–41, we used three families of models in our diagrams: shocks, photoionization from an AGN (also known as AGN narrow line region models and labeled as AGN NLR in the figures), and photoionization from hot stars. For every family of models in our diagnostic diagrams, we plot a solid outline showing the full parameter space they cover as well as a detailed grid with specific parameters that represent a narrower range of parameters that is more likely to apply to the regions of interest here. In the top two quadrants we plot grids for shock models with and without a "precursor" (see below). In the lower two quadrants we plot photoionization models for an AGN ionizing spectrum and for hot star ionizing spectra. The parameters for each model family and the detailed parameter grids are described below.

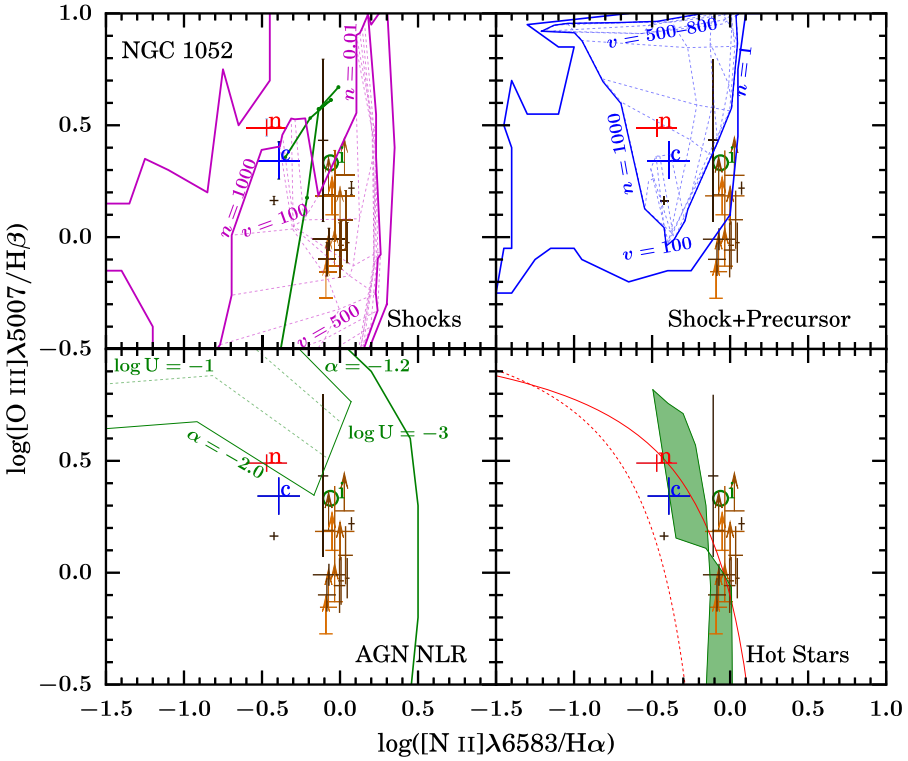

Figure 25. Diagnostic diagram of [O III]/Hβ vs. [N II]/Hα for NGC 1052. The conventions and model descriptions are the same as in Figure 24. Bottom right: same as Figure 24, except the H II region models are from Kewley et al. (2001, solid line) and Kauffmann et al. (2003, dotted line).

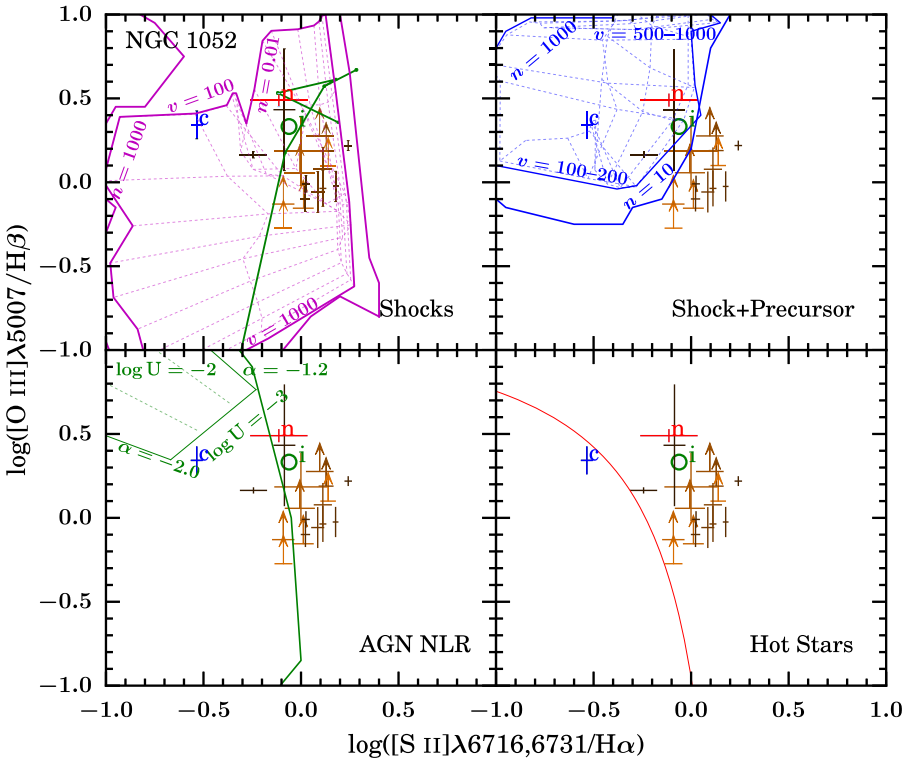

Figure 26. Diagnostic diagram of [O III]/Hβ vs. [S II]/Hα for NGC 1052. The conventions and model descriptions are the same as in Figure 24. Bottom right: same as Figure 25, except that there are no pAGB star models or H II models from Kauffmann et al. (2003).

Shocks. This family includes two types of fast shock models (with and without a precursor, for a range metallicities) from Allen et al. (2008), and slow shock models from Shull & McKee (1979). In shock models without a precursor (hereafter simple shock models) the gas is collisionally ionized by the shock while in models with a precursor ionizing photons produced in the shock-heated gas travel upstream and ionize the gas before the shock reaches it.

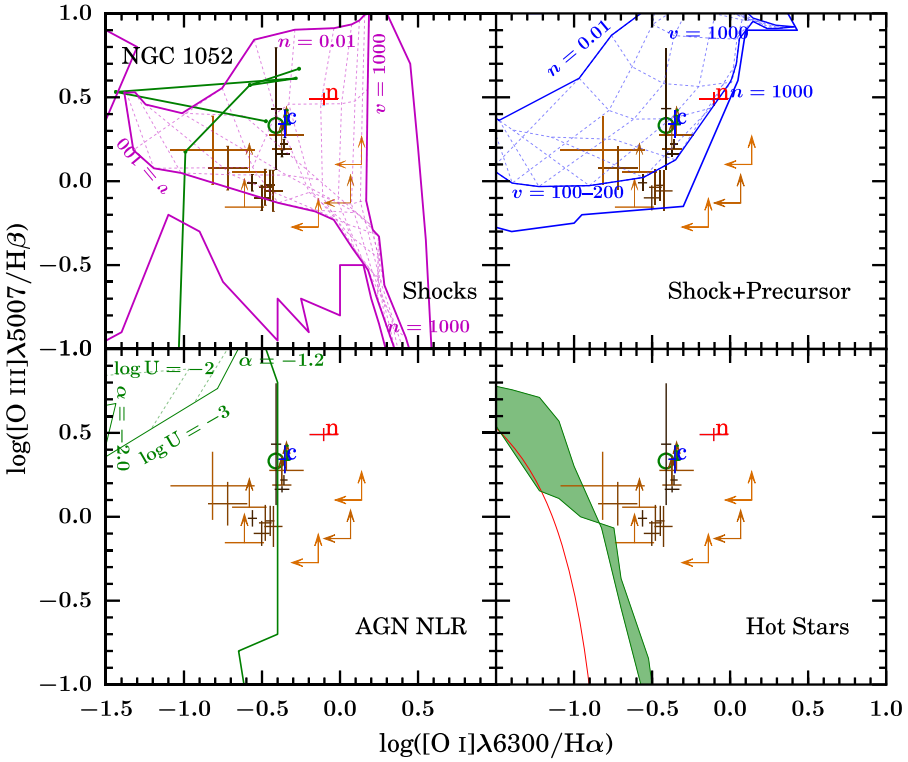

Figure 27. Diagnostic diagram of [O III]/Hβ vs. [O I]/Hα for NGC 1052. The conventions and model descriptions are the same as in Figure 24. Bottom right: same as Figure 25, but without the Kauffmann et al. (2003) H II region models.

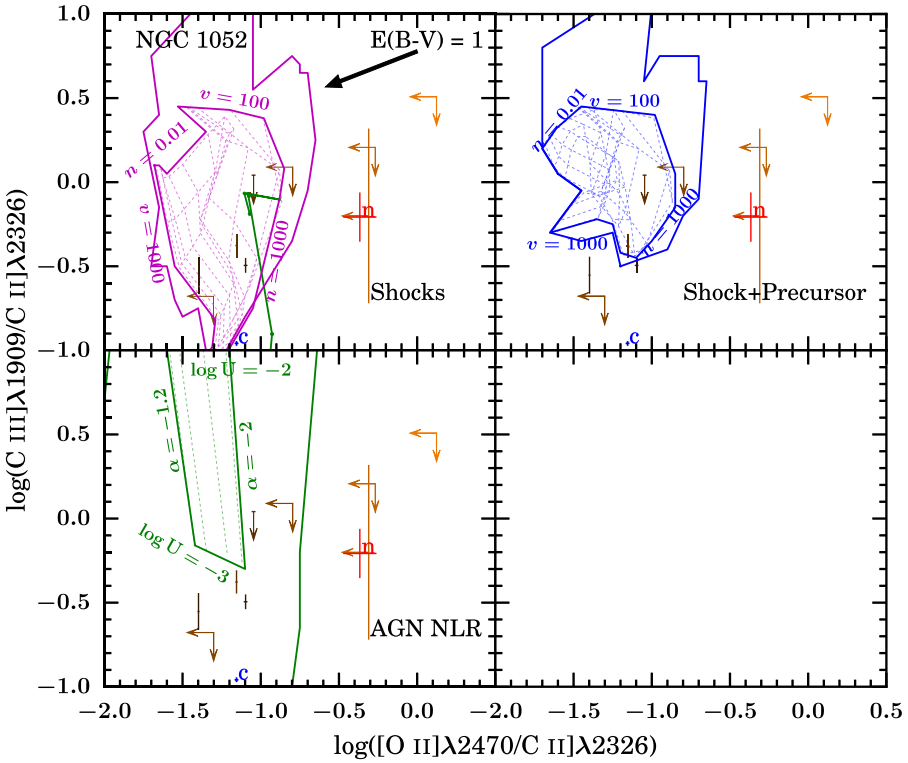

Figure 28. Diagnostic diagram of C III]/C II] vs. [O II]/C II] for NGC 1052. The conventions and model descriptions are the same as in Figure 24. Top left: same as Figure 27. The solid black arrow shows the change in the line ratios when an extinction correction of $E(B-V) = 1$ mag is applied. There are no hot star models for this diagram.

We focused on solar metallicity models, which predict line ratios for densities in the range $n = 0.1$–10^3 cm^{-3}, and twice solar metallicity models, which assume a density $n = 1$ cm^{-3}. For each of those sets, the models are calculated for magnetic field strengths in the range $B = 0.0001$–100 μG and velocities of $v = 100$–1000 km s^{-1}. The simple shock

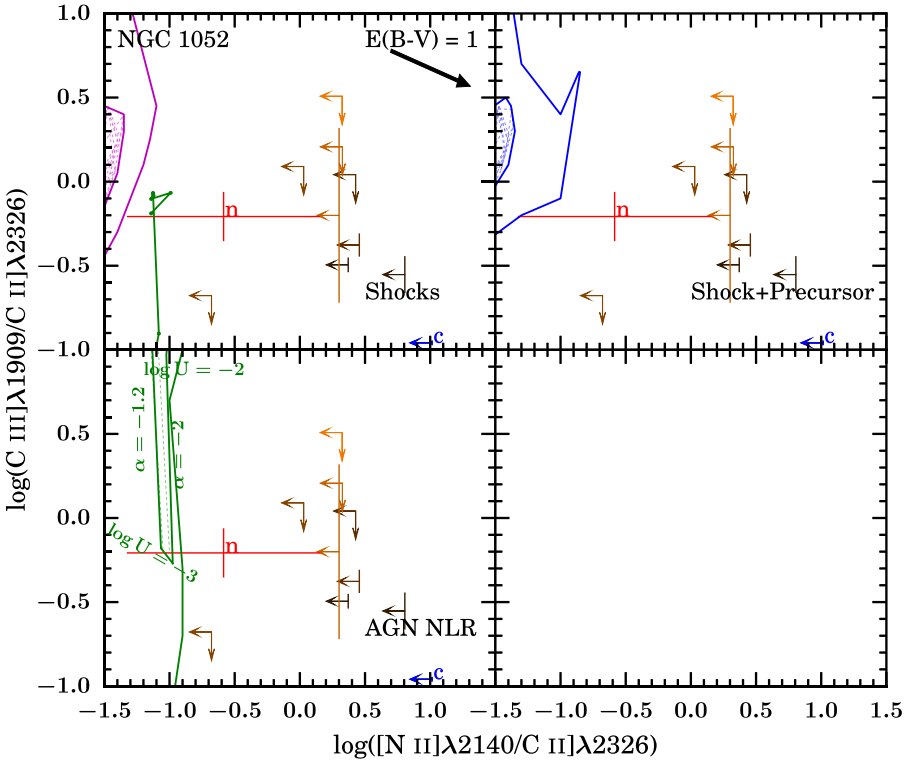

Figure 29. Diagnostic diagram of C III]/C II] vs. [N II]/C II] for NGC 1052. The conventions and model descriptions are the same as in Figure 24. There are no hot star models for this diagram.

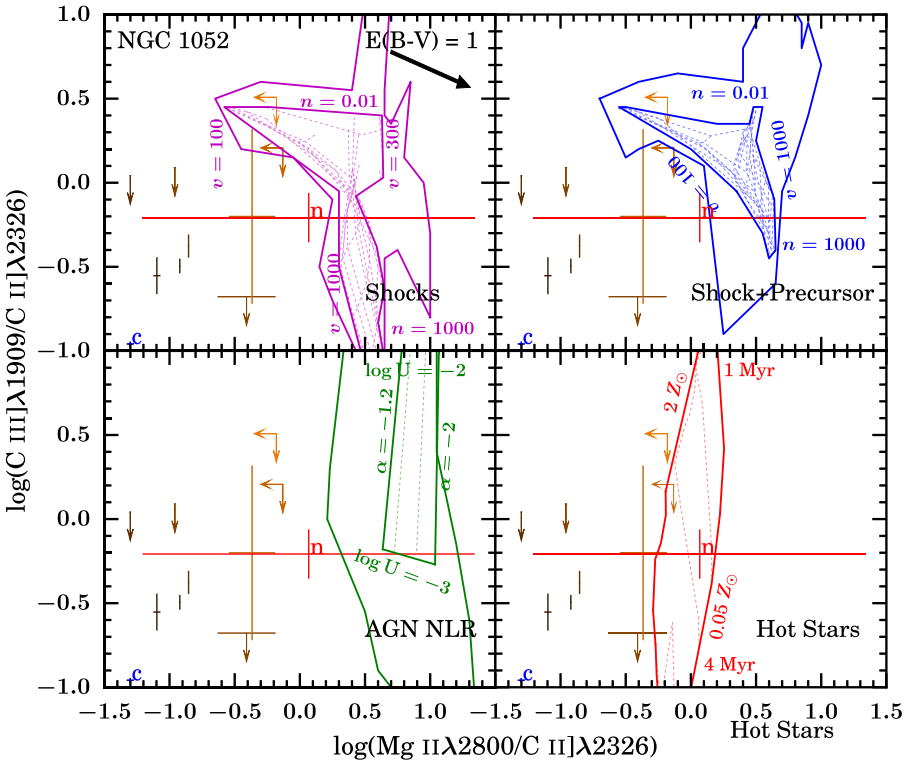

Figure 30. Diagnostic diagram of C III]/C II] vs. Mg II/C II] for NGC 1052. The conventions and model descriptions are the same as in Figure 24. Bottom right: same as Figure 24, except there are no pAGB models for this diagram.

models are shown in purple in the top left quadrant of the diagnostic diagrams, while the models of shocks with a precursor are shown in blue in the top right quadrant. The detailed grid assumes a magnetic field of $B = 1$ μG and solar metallicity, and includes the full range in density and velocity. The detailed grids were chosen to include densities similar to what was measured in Section 7, which limited us to the solar metallicity tracks. We chose $B = 1$ μG as this

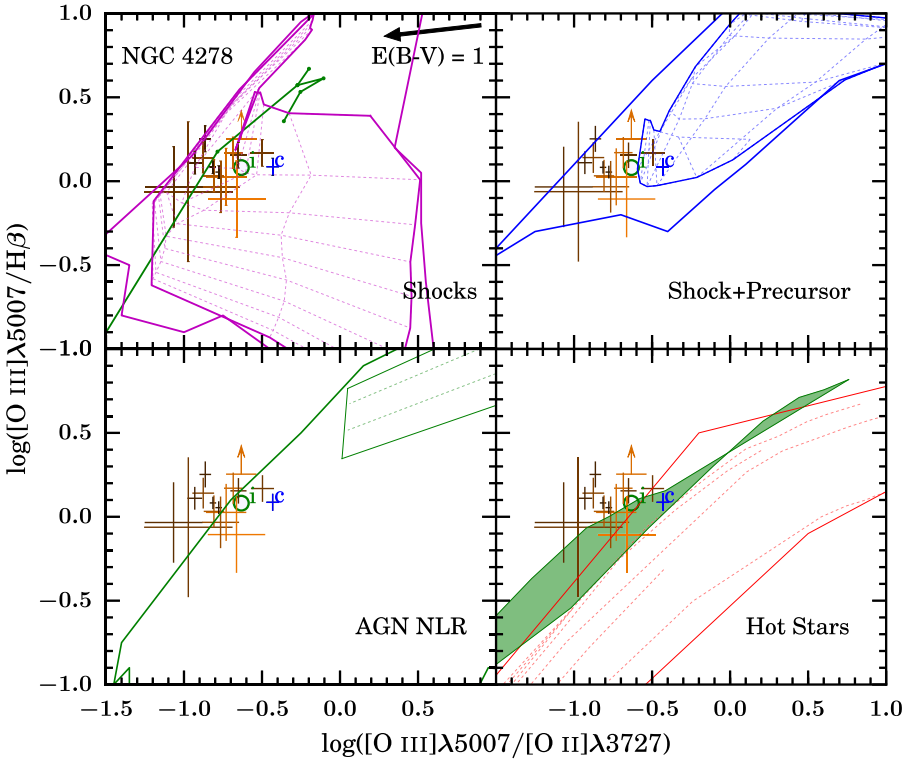

Figure 31. Same as Figure 24, but for NGC 4278. There was no unresolved source spectrum, hence no (red) "n" point is plotted.

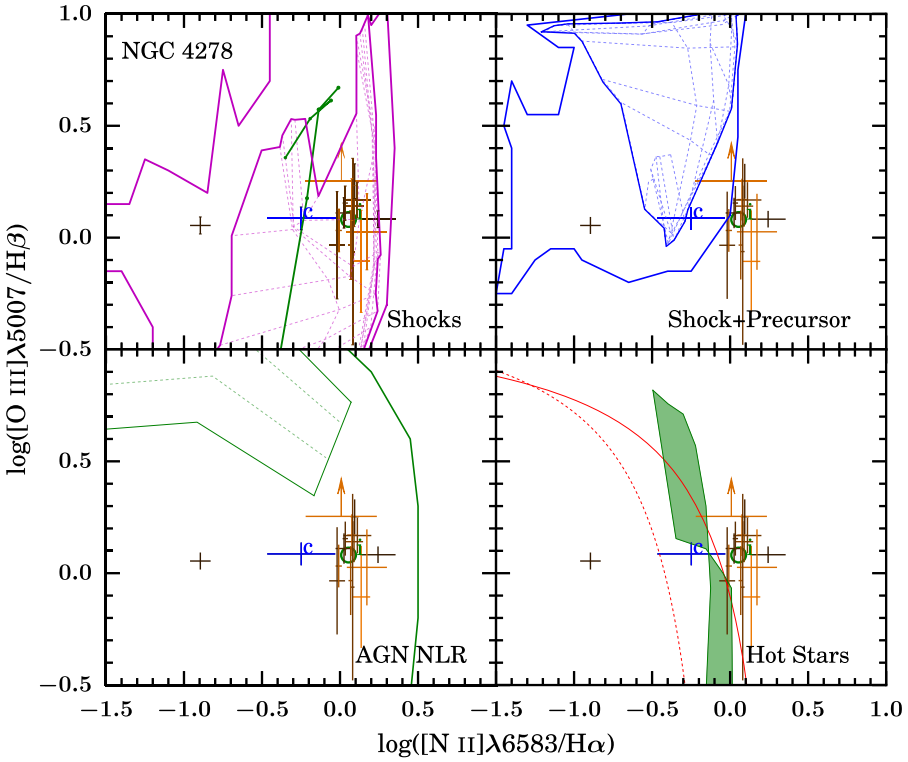

Figure 32. Same as Figure 25, but for NGC 4278. There was no unresolved source spectrum, hence no (red) "n" point is plotted.

grid overlapped with most of the tracks with magnetic fields less than 10 μG.

The slow shock models from Shull & McKee (1979) do not include a precursor and comprise two sets, one with constant density $n = 10\,\mathrm{cm}^{-3}$, "cosmic" metal abundances (see Table 2 in Shull & McKee 1979), a magnetic field of $B = 1\,\mu$G, and varying velocities of $v = 40$–$130\,\mathrm{km\,s}^{-1}$. The second set assumes the previous parameters except for a fixed velocity of $v = 100\,\mathrm{km\,s}^{-1}$, and then changes either the density to $n = 100\,\mathrm{cm}^{-3}$, the magnetic field to $B = 10\,\mu$G,

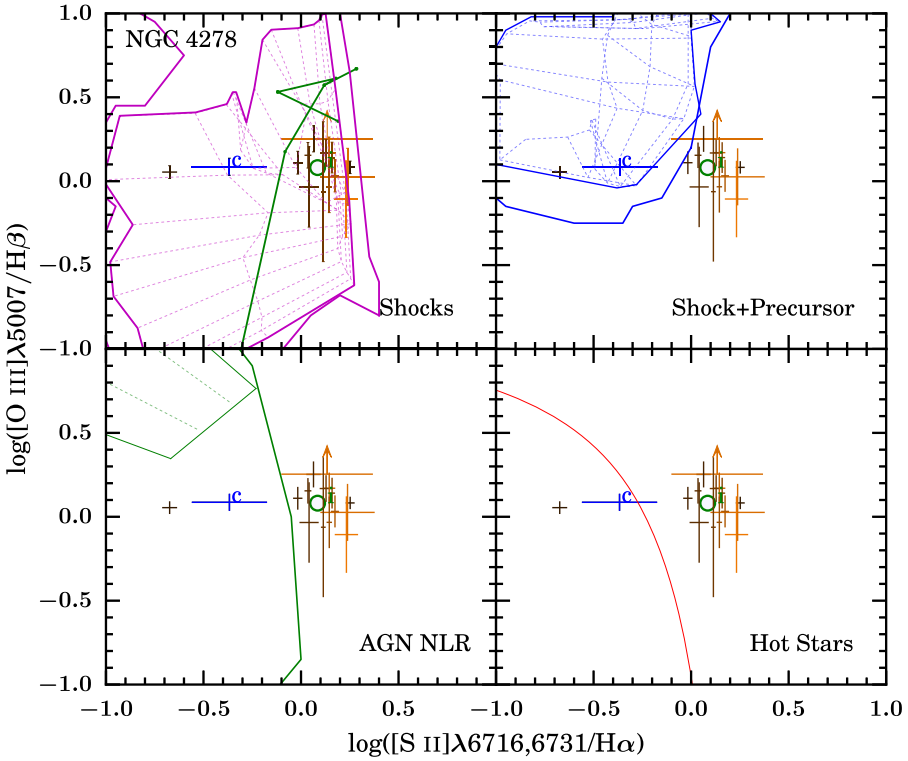

Figure 33. Same as Figure 26, but for NGC 4278. There was no unresolved source spectrum, hence no (red) "n" point is plotted.

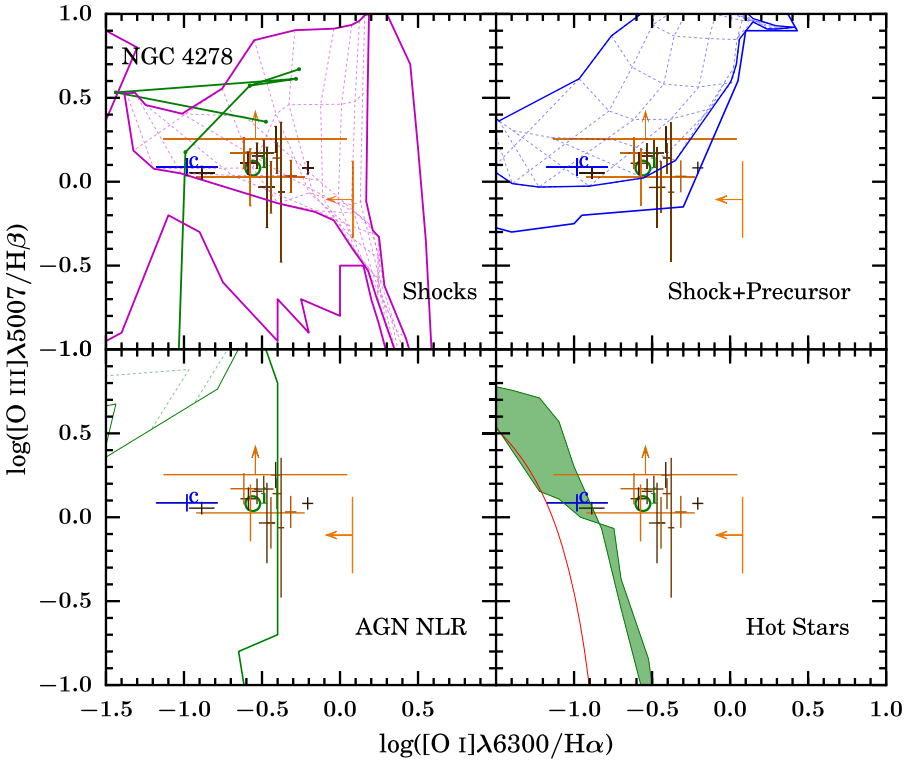

Figure 34. Same as Figure 27, but for NGC 4278. There was no unresolved source spectrum, hence no (red) "n" point is plotted.

or adopts depleted metal abundances. The slow shock models are plotted as green tracks in the top left quadrant of the diagnostic diagrams.

Photoionization by an AGN. The AGN photoionization models plotted in green in the lower left quadrant are the dust-free models from Groves et al. (2004). These models assume a simple power-law ionizing spectrum ($F_\nu \propto \nu^\alpha$, in the range 5–1000 eV) and are governed by four parameters: metallicity spanning the range $Z = 0.25$–$2\,Z_\odot$, density spanning the range

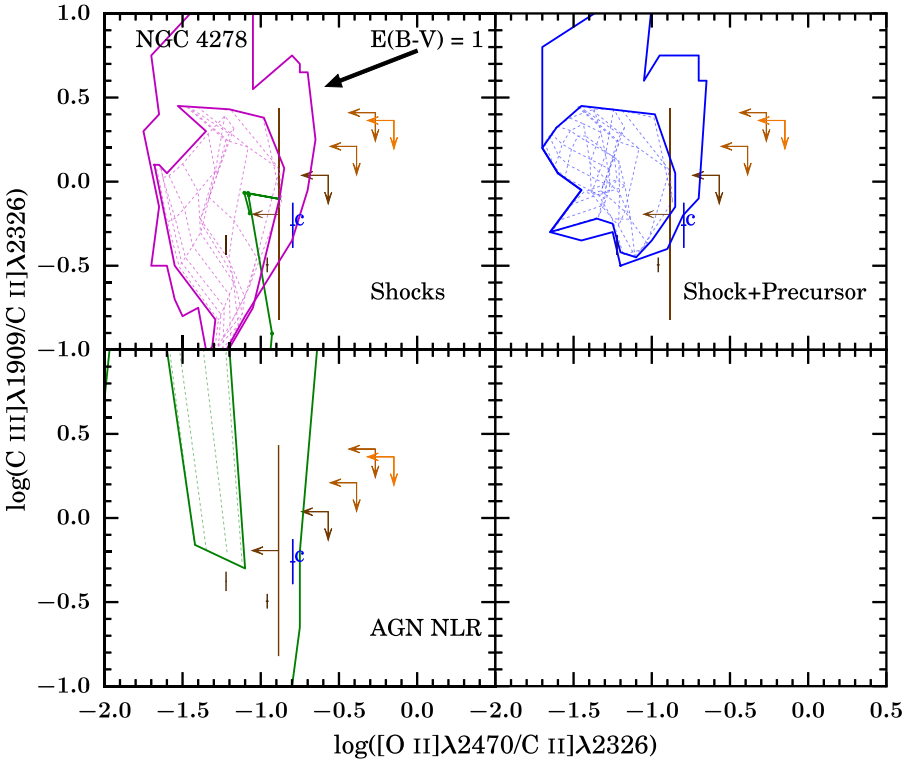

Figure 35. Same as Figure 28, but for NGC 4278. There was no unresolved component, hence no (red) "n" point is plotted. The large error bar is from the spectrum at 12 pc from the nucleus, which has a low S/N.

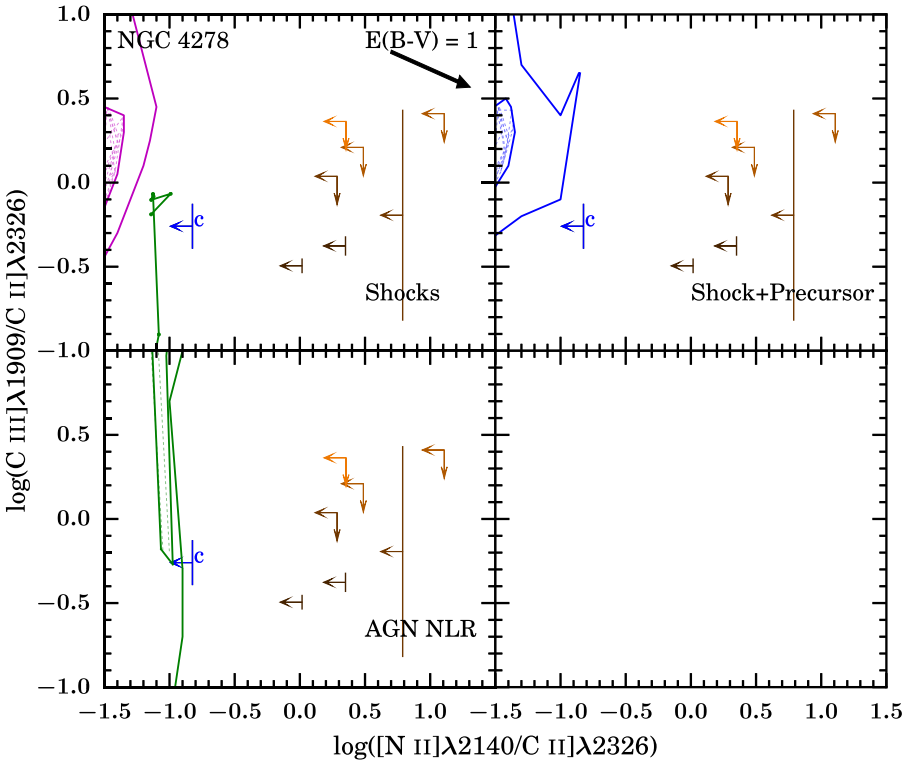

Figure 36. Same as Figure 29, but for NGC 4278. There was no unresolved component, hence no (red) "n" point is plotted. The large error bar is from the spectrum at 12 pc from the nucleus, which has a low S/N.

$n = 10^2$–$10^4\,\mathrm{cm}^{-3}$, ionization parameter[11] spanning the range $\log U = -4$ to 0, and the spectral index of the ionizing spectrum, α, spanning the range -1.2 to -2. The detailed grid assumes a constant metallicity of $Z = 2\,Z_\odot$ and density $n = 10^3\,\mathrm{cm}^{-3}$, consistent with the densities we calculated in Section 7, and the full range of

[11] See Equation (1) in Section 8.3.

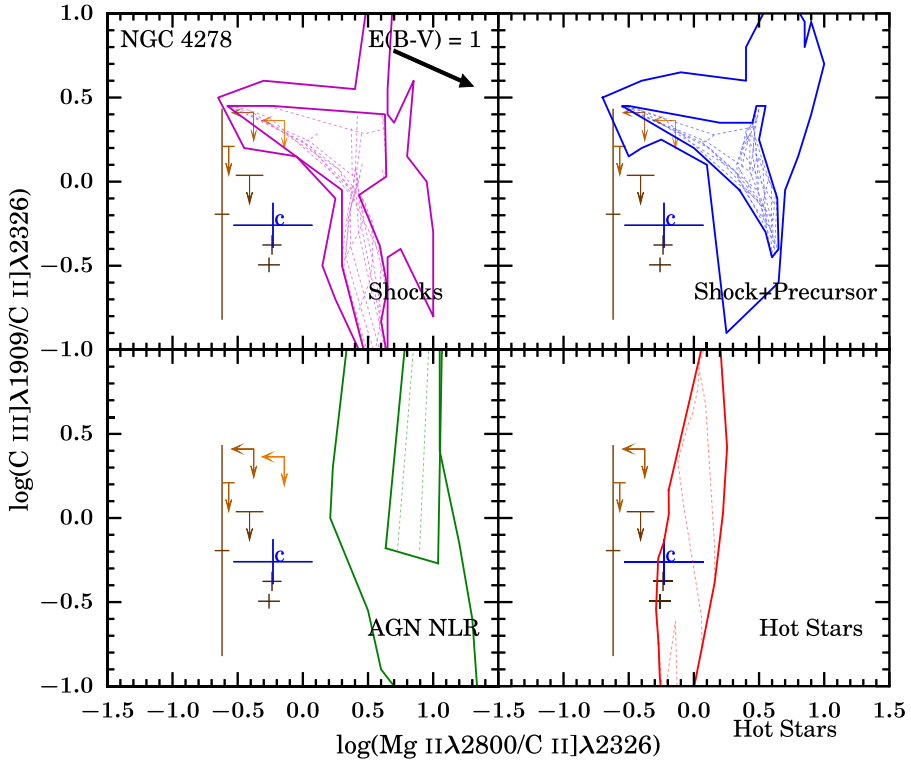

Figure 37. Same as Figure 30, but for NGC 4278. There was no unresolved component, hence no (red) "n" point is plotted. The large error bar is from the spectrum at 12 pc from the nucleus, which has a low S/N.

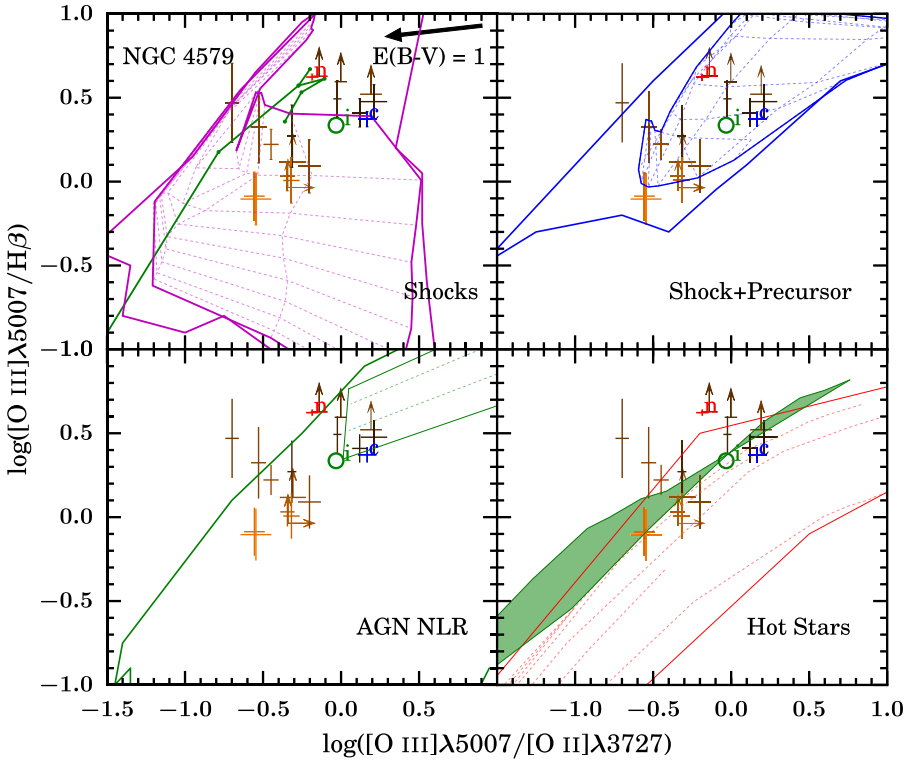

Figure 38. Same as Figure 24, but for NGC 4579.

α, but limited $\log U$ to the ranges of -3 to -1, making our grid similar to those in Kewley et al. (2006).

We compare both the RIAF and the optically thick, geometrically thin disk models of Nagao et al. (2002) to the [Ne III] λ3869/[O II] λ3727 line ratio, but do not plot them in our diagrams. While the shape of the ionizing continua are different, both models are governed by the same set of parameters: density $n = 10^{2}$–10^{5} cm^{-3}, and

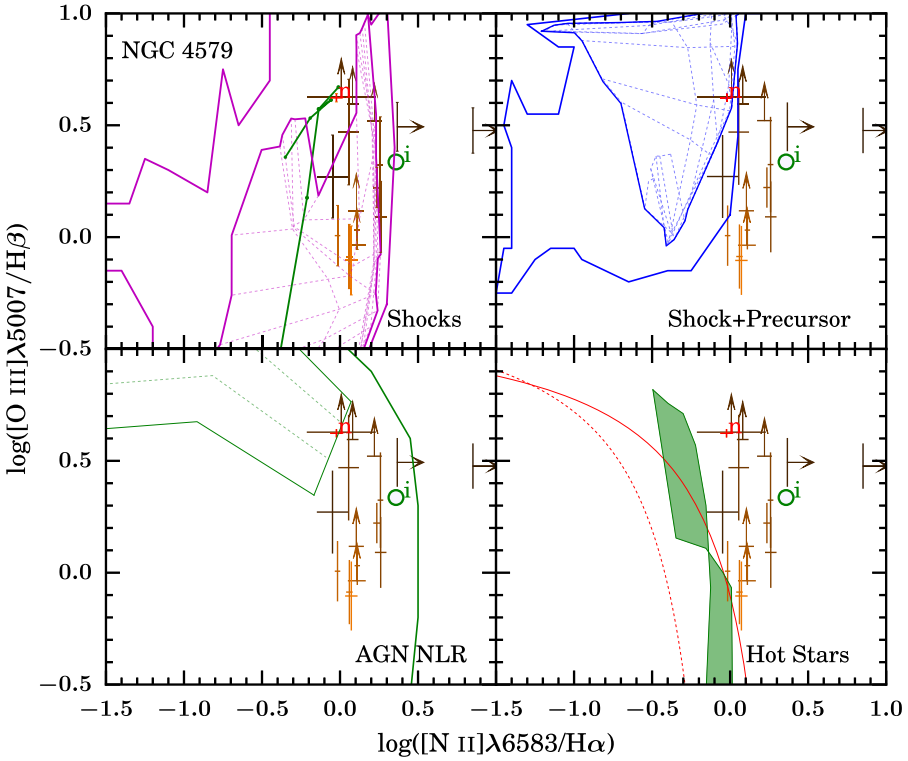

Figure 39. Same as Figure 25, but for NGC 4579. We did not measure emission line ratios from the resolved spectra within 12 pc from the nucleus due to the overwhelming strength of the unresolved nuclear source. See Section 4.1 for details.

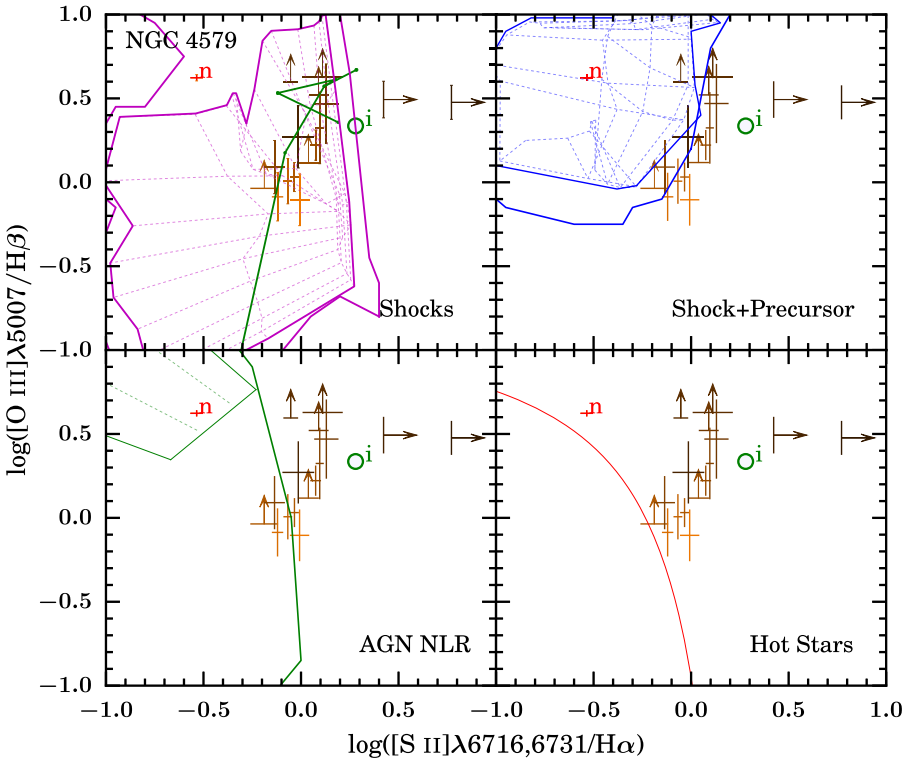

Figure 40. Same as Figure 26, but for NGC 4579. We did not measure emission line ratios from the resolved spectra within 12 pc from the nucleus due to the overwhelming strength of the unresolved nuclear source. See Section 4.1 for details.

ionization parameter $\log U = -4$ to -1.5. The RIAF models use a spectral energy distribution (SED) template from Kurpiewski & Jaroszyński (1999) which has no thermal blue/UV component (i.e., "big blue bump"), and employs a simple power-law ionizing continuum ($f_\nu = \nu^{-0.89}$ with exponential cutoffs at 10^{-4} and 10^4 Ry). The optically thick, geometrically thin disk model is empirical, and has a more complex SED

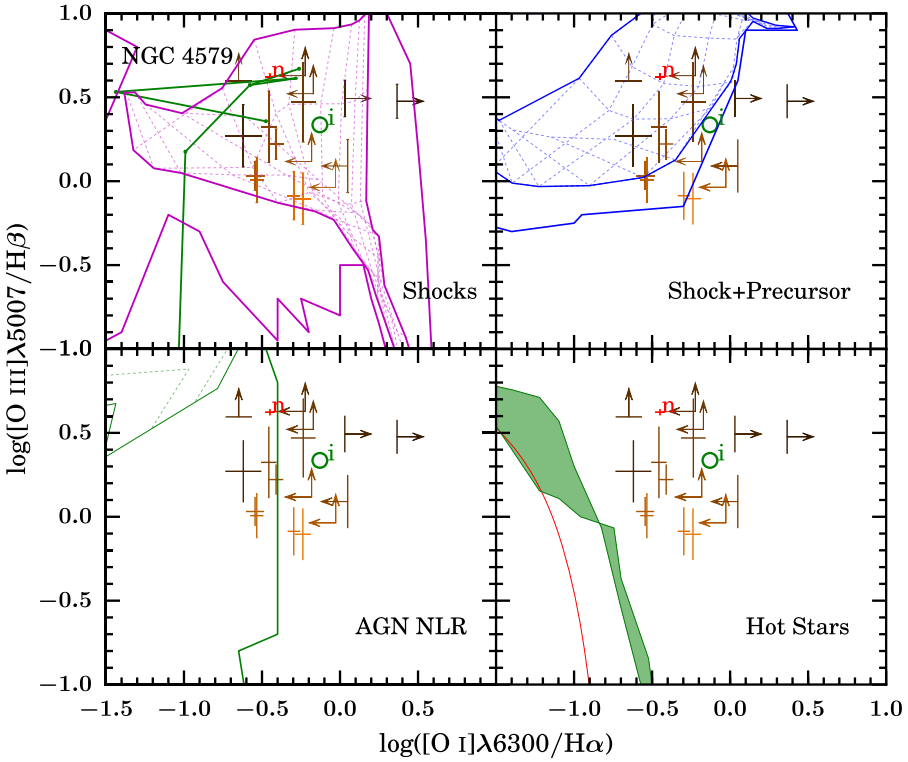

Figure 41. Same as Figure 27, but for NGC 4579. We did not measure emission line ratios from the resolved spectra within 12 pc from the nucleus due to the overwhelming strength of the unresolved nuclear source. See Section 4.1 for details.

(as described in Equation (1) of Nagao et al. 2002). Its distinguishing characteristics include a big blue bump with a characteristic temperature of 4.9×10^5 K, and a power law of the form $f_\nu \propto \nu^{-3}$ from 100 keV to 10^4 Ry.

Photoionization by hot stars. The hot star models include pAGB stars from Binette et al. (1994), and H II models from Dopita et al. (2006) and Kewley et al. (2006). These models are shown in the lower right quadrant of the diagnostic diagrams, with the pAGB models represented by the green shaded regions and the H II models in red. The Binette et al. (1994) pAGB models are based on a 13 Gyr stellar population (except for the $Z = 1\,Z_\odot$ model, which includes both 8 and 13 Gyr populations), and are described by two parameters: metallicity spanning $Z = \frac{1}{3} - 3\,Z_\odot$ and ionization parameter spanning $\log U = -3$ to -5. The density is assumed to be $n = 10^3\,\mathrm{cm}^{-3}$. The age of this population allows for light from pAGB stars to be the dominant source of ionizing photons, which produces an ionizing continuum similar to a blackbody of $T \approx 10^5$ K (see Binette et al. 1994 for more details). The pAGB models are only used in three out of the seven diagrams as they do not predict the relative intensities of the NUV lines or [S II] λλ6716, 6731. Their main difference compared to the H II region models described below is the higher temperature of the stars providing the ionizing photons.

We use H II region models from two sources. The [O III]/Hβ versus [O III]/[O II] and C III]/C II] versus Mg II/C II] diagrams use models from Dopita et al. (2006), which cover a population age from 0.2 Myr to 4 Myr and metallicity $Z = 0.2$–$2\,Z_\odot$. The Dopita et al. (2006) models are characterized by the central cluster mass (100–$10^6\,M_\odot$) and interstellar medium pressure (10^4–$10^7\,\mathrm{cm}^{-3}$ K, corresponding to $n \sim 1$–$10^3\,\mathrm{cm}^{-3}$), and have an ionizing continuum dominated by stars with an effective temperature $T_{\rm eff} \approx 10^{4.5}$ K. The models from Kewley et al. (2006), which include both the theoretical extreme starburst line from Kewley et al. (2001) and the empirical composite objects line from Kauffmann et al. (2003), are shown in the [O III]/Hβ versus [N II]/Hα, [S II]/Hα, and [O I]/Hα diagrams. The Kewley et al. (2001) models include both instantaneous burst as well as continuous star formation models. These models yield the maximum line ratios that can be explained by stellar photoionization, and are denoted by a solid line in the relevant diagnostic diagrams.

8.3. Comparison of Models with the Data for Individual Galaxies

It is evident from the diagnostic diagrams that there is considerable degeneracy between the models. Therefore we seek the models that offer the best explanation of the data, i.e., those that explain most of the diagnostic diagrams. In the discussion below we note what range of model parameters is needed in order for the models to explain the data.

To aid us in the assessment of the AGN photoionization models, we compute the ionization parameter due to ionizing radiation from the AGN as a function of distance from the center of the galaxy via

$$U = \frac{Q}{4\pi r^2 nc}, \quad (1)$$

where Q is the rate of emission of hydrogen-ionizing photons, r is the physical distance from the nucleus, and n is the hydrogen density. We adopt the values of Q obtained by Eracleous et al. (2010a) by integrating the observed SED and take the electron density from Section 7 as a proxy for the hydrogen density,

accepting that there is an uncertainty of less than a factor of 2, which does not affect our conclusions.

By inspecting the diagnostic diagrams we can readily see that hot star models cannot explain the data for any of the galaxies and at any distance from the center of the galaxy. The [O I]/Hα ratio proves particularly useful in discriminating against hot star photoionization models. The other families of models have a varying degree of success as we detail below.

NGC 1052, Figures 24–30. All but the C III]/C II] versus O II]/C II] diagram show that the emission from the unresolved nuclear source can be explained with the shock plus precursor model, but the required density, $n = 10^{-2}$–10^{2} cm^{-3}, is lower than that inferred from the [S II] $\lambda\lambda$6716, 6731 doublet (Section 7), which disfavors this family of models. Similarly, the simple shock models agree with the data in five of the seven diagrams, but the required density is the same as the shock plus precursor models, disfavoring all shock models for the unresolved nuclear source emission for NGC 1052. Photoionization from an AGN agrees with the data in five of the seven diagrams as long as $-1.9 \leqslant \alpha \leqslant -1.2$, $-3 \leqslant \log U \leqslant -2.8$, $Z = 2$–$4\,Z_{\odot}$, and $n = 10^{3}$–10^{4} cm^{-3}.

In six of the seven diagrams, the line ratios of the spatially resolved spectra can be explained by simple shock models with $Z = 1$–$2\,Z_{\odot}$, $n = 10^{-2}$–10^{2} cm^{-3}, $B = 0.5$–$18\,\mu$G, and velocities $v = 100$–500 km s^{-1}. Photoionization from an AGN explains the data in four out of the seven diagrams, as long as $-1.9 \leqslant \alpha \leqslant -1.2$, $-3.65 \leqslant \log U \leqslant -3.4$, $Z = 1$–$2\,Z_{\odot}$, and $n = 10^{2}$–10^{4} cm^{-3}. The shock plus precursor models agree with the data in four out of the seven diagrams, as long as $Z = 1$–$2\,Z_{\odot}$, $B = 0.2$–$32\,\mu$G, $v = 100$–500 km s^{-1}, and $n = 10^{-2}$–10^{2} cm^{-3}. The densities required by the simple shock and the shock plus precursor models are consistent, within uncertainties, with the values inferred from the [S II] doublet ratio.

The spatially resolved nuclear emission often follows the spatially resolved extended emission as described above, except for Figures 25 and 26. When these diagrams are taken into account, the spatially resolved nuclear emission is consistent with simple shock models in five out of the seven diagrams, as long as $B = 0.5\,\mu$G, $v = 100$–300 km s^{-1}, $n = 10^{-2}$–10^{3} cm^{-3}, and $Z = 1\,Z_{\odot}$. Photoionization from an AGN explains the data in five out of the seven diagrams, as long as $-1.9 \leqslant \alpha \leqslant -1.2$, $-3.6 \leqslant \log U \leqslant -3.4$, $Z = 1$–$2\,Z_{\odot}$ and $n = 10^{2}$–10^{3} cm^{-3}. The shock plus precursor models also agree with the data in five out of the seven diagrams, as long as $B = 0.2 - 16\,\mu$G, $v = 300$–400 km s^{-1}, $n = 10^{-2}$–10^{3} cm^{-3}, and $Z = 1\,Z_{\odot}$.

The upper limits for [Fe X] λ6374 and [Fe XIV] λ5303 agree with shock models from Wilson & Raymond (1999) for $v = 200$–350 km s^{-1}. The [Ne III]/[O II] line ratio near the nucleus are consistent with both families of AGN photoionization models of Nagao et al. (2002).

NGC 4278, Figures 31–37. The spatially resolved spectra can be explained by simple shock models with $Z = 1$–$2\,Z_{\odot}$, $n = 10^{-2}$–10^{3} cm^{-3}, $B = 0.15$–$20\,\mu$G, and $v = 100$–500 km s^{-1}. The line ratios from the spatially resolved spectra can also be explained by shock plus precursor models in five of the seven diagrams, with $Z = 1$–$2\,Z_{\odot}$, $n = 10^{-2}$–10^{3} cm^{-3}, $B = 1$–$1000\,\mu$G, $v = 100$–500 km s^{-1}. Models of photoionization by an AGN agree with the data in five of the seven diagrams, as long as $-2.0 \leqslant \alpha \leqslant -1.75$, $-3.65 \leqslant \log U \leqslant -3.45$, $Z = 0.5$–$2\,Z_{\odot}$ and $n = 10^{2}$–10^{3} cm^{-3}. The point representing the nuclear spectrum of NGC 4278 is often separated from the other data points in the diagnostic diagrams, and agrees with almost all models. We will discuss this point further in Section 9.1.

The upper limits for [Fe X] λ6374 and [Fe XIV] λ5303 agree with shock models from Wilson & Raymond (1999) for $v = 200$–350 km s^{-1}. We could not detect [Ne III]/[O II]. The values of $\log U$ change from ≈ -1 close to the nucleus to ≈ -3 at 30 pc from the nucleus.

NGC 4579, Figures 38–41.The NUV spectrum is dominated by the light from the AGN, so we consider only the four optical diagnostic diagrams for this galaxy. In all diagrams, the line ratios from the spatially unresolved nuclear source can be explained by the simple shock and shock plus precursor models with $Z = 1$–$2\,Z_{\odot}$, $n = 0.1$–320 cm^{-3}, $B = 0.0001$–$40\,\mu$G, and $v = 300$–800 km s^{-1}, but the low density required disfavors these models given the density estimate described in Section 7. Photoionization by an AGN can explain the data in three of the four diagrams, if $-1.8 \leqslant \alpha \leqslant -1.2$, $-3.2 \leqslant \log U \leqslant -2.7$, $Z = 0.5$–$4\,Z_{\odot}$, and $n = 10^{2}$–10^{4} cm^{-3}.

In all diagnostic diagrams, the line ratios from the spatially resolved spectra can be explained by simple shock models with $Z = 1$–$2\,Z_{\odot}$, $n = 10^{-2}$–10^{3} cm^{-3}, $B = 0.0001$–$40\,\mu$G, and $v = 100$–500 km s^{-1}. The upper limits for [Fe X] λ6374 and [Fe XIV] λ5303 agree with shock models from Wilson & Raymond (1999) for $v = 200$–350 km s^{-1}.

The [Ne III] λ3869 line is detected only very close to the nucleus; when this line is detected the [Ne III]/[O II] ratio agrees with the predictions of photoionization models for both families of AGN models described in Nagao et al. (2002). Our estimated value of $\log U$ drops from ≈ -2 near the nucleus to ≈ -3.8 at $\approx$80 pc from the nucleus.

Our conclusion is that simple shock models can explain the relative strengths of most of the emission lines from regions we can resolve, i.e., on scales of a few parsecs or more in NGC 1052 and NGC 4579. NGC 4278 is strongly affected by the small-scale jets associated with its AGN, and will be discussed in more detail in Section 9.1. The only exceptions are the C III]/C II] versus Mg II/C II] diagrams, in Figures 30 and 37, where the data are in poor agreement with all the models. However, the model results for the Mg II λ2800 doublet, the only resonance lines that we use here, should be regarded with caution. They were obtained with the MAPPINGS III code, which does not evaluate multiple scatterings for resonance lines and ensuing attenuation. Thus, the strength of the Mg II λ2800 doublet could be overestimated, as described in Groves et al. (2004). The above conclusion is corroborated by the kinematics of the line-emitting gas, presented in Section 6.3. The velocity of the gas is similar to the shock velocities needed to explain the relative strengths of the lines. Thus, the picture is reminiscent of the case of M87 where the gas within the central $\sim$20 pc is photoionized (Sabra et al. 2003), while the off-nuclear gas is arranged in a disk and the lines appear to be the result of shock excitation (Dopita et al. 1996, 1997).

The line ratios measured from the integrated spectra of all three objects fall in regions of the diagnostic diagrams that can be described by more than one model. In view of the conclusions above we can attribute this ambiguity to the fact that the large ($\sim$100 pc size) region probed by the integrated

spectrum includes a mixture of photoionized gas and gas excited by shocks.

The [S II]/Hα ratio and, to some degree, also the [N II]/Hα and [O I]/Hα ratios, provide crucial constraints on the models for the excitation of the line-emitting gas. Our preference for shock models is based largely on their ability to reproduced the observed values of these ratios when other models cannot. Because of the importance of the [S II]/Hα ratio, we examine more carefully the predictions for its value made by a variety of photoionization models. We observe this ratio to be clustered around 1.0 in NGC 1052 and around 1.2 in NGC 4278, and to span the range 1.0–1.4 in NGC 4579. These values are too large for AGN NLR models to explain, regardless of what the other line ratios (or physical parameters) are. Because of these large values, *composite* photoionization involving a range of densities and ionization parameters from the sets that we tested (see Barth et al. 1996) cannot reproduce [S II]/Hα ratios as high as those observed. The dusty, isobaric models of Dopita et al. (2002) and Groves et al. (2004) can produce such high values of [S II]/Hα for $\log U \approx -3$ but they cannot simultaneously reproduce the [N II]/Hα and [O III]/Hβ ratios. The Ho et al. (1993) models can reproduce the observed values [S II]/Hα for $\log U \approx -4$ but they require $n < 10^3\,\mathrm{cm}^{-3}$, in contradiction with what we infer from the relative strengths of the lines in the [S II] $\lambda\lambda$6716, 6731 doublet. The models of Binette et al. (1996) and their extension by Sabra et al. (2003) employ a mix of ionization-bounded and matter-bounded clouds and can only reproduce the observed [S II]/Hα for very low densities of $n \sim 50\,\mathrm{cm}^{-3}$, which does not agree with the density constraints from the lines in the [S II] $\lambda\lambda$6716, 6731 doublet.

We further compared the measured [O I]/[O III], [O II]/[O III], and [S II]/[O III] line ratios of the spatially unresolved nuclear source in NGC 1052 and NGC 4579 to the two families of photoionization models in Nagao et al. (2002). We found that these ratios fall in the regions of the diagnostic diagrams where the predictions of the RIAF and optically thick, geometrically thin disk models overlap given the densities inferred from the [S II] doublet ratio. Thus we cannot distinguish between the models for the SED of the ionizing continuum based on the data presented here (see Maoz 2007; Ho 2008; Eracleous et al. 2010b; Nemmen et al. 2014, and references therein for a discussion of SED shapes and models).

We conclude our comparison of the data with models by noting an important caveat. All the models that we have compared with the data are "single-zone" models, i.e., they employ fixed values of their physical parameters. However, it is quite possible that the spatial bins from which we extracted the spectra include gas with a range of densities and other parameters. This is most likely in the central parts of each galaxy where the density gradient is high. It is also possible that photoionized and shocked gas co-exist. Our understanding of the physical processes can, therefore, be advanced by constructing "multi-zone" and "multi-process" models and comparing them to the data.

9. Discussion

The LINER-like spectra of the galaxies in our sample appear to result from a combination of photoionization from the AGN and shocks. In NGC 1052 and NGC 4579, the two cases where we isolated the spatially unresolved nuclear light from the extended, resolved light, we found a transition from photoionization by an AGN to excitation by shocks at ~20 pc from the nucleus. Below, we consider physical interpretations for each galaxy and then discuss implications for the LINER population as a whole.

9.1. Physical Interpretation of Diagnostic Diagrams

NGC 1052. The emission from the spatially unresolved nuclear source is best explained by photoionization from the AGN. In five out of the seven diagrams there is good agreement between the data and AGN photoionization models, within uncertainties, while all other models are disfavored by the low densities required in order for other model families to explain the data.

The extended, resolved emission from NGC 1052 is consistent with excitation by shocks with velocities around 300–500 km s^{-1}. Previous studies (Pogge et al. 2000; Walsh et al. 2008) found evidence for strong outflows and ionized regions associated with jet-like features. Studies that incorporate radio observations found strong evidence for shocks in a turbulent, rotating disk on both parsec and sub-parsec scales, suggesting that the jet is interacting with the circumnuclear gas (Sugai et al. 2005; Dopita et al. 2015).

In view of the jet–disk interaction, the spectrum of the spatially resolved nuclear source may contain some contributions from shocked gas, not just gas that is photoionized by the AGN. Indeed, we see that five of the seven diagrams for this galaxy have spatially resolved nuclear emission line ratios that agree with the AGN photoionization models. We also find that five of the seven diagrams of the spatially resolved nuclear source also agree with the shock plus precursor models, which is consistent with the turbulent rotating disk idea presented in Sugai et al. (2005) and Dopita et al. (2015). The ambiguity in the explanations for the spatially resolved nuclear emission could imply that the source of the shocked gas could be very close to the central engine in this galaxy.

NGC 4278. All of the observed emission line ratios are well described by shocks with velocities of 100–500 km s^{-1}, except for the central spectrum of the resolved light, which agrees with simple shock, shock plus precursor, and AGN photoionization models. While the presence of jets indicates that there is an AGN in NGC 4278, the inferred ionization parameter we obtain in Section 8.3 ($\log U \approx -1$) is considerably different than than that required for AGN photoionization models to reproduce the diagnostic diagrams ($\log U \approx -3$). This mismatch calls into question photoionization from the AGN as an explanation for the observed line ratios and leads us to favor shock models as a better explanation of the observed spectra. We speculate that our direct view of the gas that is photoionized by the AGN is obscured.

NGC 4278 is well known to have sub-parsec scale jets (Giroletti et al. 2005; Helmboldt et al. 2007) which lie completely within the slit used in our observations, as well as a warped velocity field within 0.″5 (Walsh et al. 2008). Giroletti et al. (2005) found that the jets in NGC 4278 have a similar structure to those seen in radio-loud AGN, but are disrupted before reaching kiloparsec scales. We conclude the shocks created by the disrupted jets are responsible for powering the emission lines from the gas that we can observe directly.

NGC 4579. The unresolved nuclear emission is best explained by photoionization from the AGN. In three out of the four diagnostic diagrams there is good agreement between the data and AGN photoionization models. The only diagram in which agreement is marginal is the [O III]/Hβ versus [O III]/[O II] diagram (Figure 38), where the data and models can be brought into agreement by a small adjustment of the extinction correction. The value of log U we determine in Section 8.3 agrees with the value required by the photoionization models. We note that the models of Groves et al. (2004) do not encompass the value of α that is measured for NGC 4579 ($\alpha \approx -0.9$; Eracleous et al. 2002), which is another possible cause of the small discrepancy between the models and the data in this diagram. Our conclusion that AGN photoionization is the dominant mechanism in the unresolved nuclear source is corroborated by the NUV spectrum in Figure 7, which includes broad lines and a featureless continuum, just as in an a luminous active galaxy.

The resolved emission is only consistent with simple shock models with velocities around 100–500 km s^{-1}. While jets are not clearly detected in this object, previous studies have suggested that jets are responsible for the sub-parsec radio emission seen in NGC 4579 (Falcke et al. 2000; Ulvestad & Ho 2001, and references therein). Additionally irregular gas rotation was found both in the central 1″ (Walsh et al. 2008), as well as at larger scales (Gonzalez Delgado & Perez 1996). Thus it appears possible that there is an outflow from the AGN that interacts with circumnuclear gas.

9.2. Implications for the LINER Population

We find that, in order to completely describe the emission line spectra of the three LINERs in our small sample we must invoke a combination of photoionization from the AGN and excitation by shocks at larger distances from the nucleus, in agreement with previous work on M87 by Dopita et al. (1997) and Sabra et al. (2003). Both of these processes are ultimately associated with the AGN and derive their power from accretion onto the central supermassive black hole. The idea that AGNs can interact with their surroundings in other ways besides photoionization is not new (Cecil et al. 1995; Capetti et al. 1997; Falcke et al. 1998; Ferruit et al. 1999; Dopita 2002 e.g.,), but it does not always receive its due attention because photoionization is the dominant mechanism producing the emission lines in more luminous AGNs (Laor 1998).

Conversely, discussions of the power sources of LINERs typically seek an explanation in terms of a single mechanism (see Ho 2008 and references therein), but often a single mechanism does not provide a complete explanation of the observed line strengths. For example, photoionization from an AGN often does explain the *relative* line strengths but not the energy budget (e.g., Flohic et al. 2006; Eracleous et al. 2010a, and references therein). The central engines in our objects have properties similar to a less luminous, accretion-powered engine, whose lower luminosity allows the contribution from shocks to become non-negligible as predicted by Laor (1998).

Thus, we conclude that for LINERs that have an AGN, the effect of shocks caused by jets or other types of outflows cannot be ignored. Another possibility is that energetic particles emanating from a RIAF (Narayan & Yi 1995; Blandford & Begelman 1999) may deposit their energy in circumnuclear gas and produce emission lines with relative intensities similar to shocks. The shocks and photoionization (and perhaps other processes) will combine in delivering energy to the line-emitting gas, which means the models relying on just one of these mechanisms will not adequately describe the observed emission lines. The relative contributions of shocks and photoionization to the power budget will depend on the individual properties of the AGN and vary from object to object. As we noted in Section 1, there is no way to assess quantitatively the contribution of jets to the power budget, and therefore we cannot determine whether the jets are powerful enough to explain the emission line luminosities. Hence we must infer how much they contribute from the emission line ratios and by spatially resolving and separating the regions where different excitation mechanisms dominate.

Clearly, the combination of AGN photoionization and AGN-driven shocks will not apply to all objects. The LIERs in non-active galaxies studied by Yan & Blanton (2012), Belfiore et al. (2016), and others, reside in galaxies without an AGN and represent emission from most of the volume of the galaxy. In such cases photoionization by hot stars, especially pAGB stars, is an essential process to consider since an AGN is not a plausible power source (e.g., Binette et al. 1994; Papaderos et al. 2013; Singh et al. 2013). By extension, pAGB stars may also be the source of ionizing photons that power the line emission in nearby LINERs, as noted by Ho (2008) and Eracleous et al. (2010a). The photoionization may be accompanied by shocks from the fast winds of pAGB stars and proto-planetary nebulae (e.g., Bujarrabal et al. 1998; Sevenster & Chapman 2001; Van de Steene & van Hoof 2003) with theoretically predicted speeds reaching several hundred km s^{-1} (e.g., Frank & Mellema 1994). Thus the combination of line emission mechanisms observed in LINERs may also apply to LIERs, although the origin of the ionizing photons and shocks is different.

10. Summary

In this work, we have analyzed spatially resolved spectra of three nearby luminous LINERs: NGC 1052, NGC 4278, and NGC 4579. The spectra sample the compact nuclear emission line regions with a spatial resolution of better than 10 pc. All three objects have multiple indicators of an AGN, as well as observed Hα line strengths on the scale of $\sim$100 pc that cannot be explained by photoionization from the AGN alone (Eracleous et al. 2010a). To amass a wide range of diagnostic lines on small spatial scales, we obtained new spectra in the blue (2900–5700 Å) and NUV (1570–3180 Å) bands and combined them with archival red spectra (6300–6860 Å) from Walsh et al. (2008) obtained with a similar *HST* setup .

In order to separate the resolved light from the bright nucleus, we decomposed the 2D spectra into a spatially unresolved nuclear source and an extended, resolved source for NGC 1052 and NGC 4579. We attempted a similar decomposition with NGC 4278, but we found that the strength of the spatially unresolved nuclear source was statistically consistent with zero. We also created an "integrated" spectrum, which emulates what might be observed from a ground-based telescope.

We measured and compared diagnostic emission line ratios from the spectra of the extended resolved light, the spectrum of the spatially unresolved nuclear source, and integrated spectrum to models for different excitation mechanisms: shocks, photoionization from an AGN, and photoionization by hot stars (young and old). The physical model that best describes the data comprises an AGN that photoionizes the gas near the nucleus and shocks that ionize the gas at larger distances from the nucleus. The relative importance of the photoionization and shocks depends on the properties of the AGN and the source of the shocks, which varies from object to object. In the LINERs of our small sample the luminosity of the AGN is low enough that it does not overpower excitation by shocks. This physical model will not apply in cases of extended LIERs or passive red galaxies. In such galaxies, photoionization from pAGB stars and, perhaps, shocks associated with outflows from these stars may be responsible for the observed emission line spectra.

In closing, we note that a single mechanism may not fully explain observed line strengths in LINER emission on scales of order 100 pc or larger. Similarly, to fully understand the power source of extended LIERs, spatially resolved spectra are required to track any changes in the excitation mechanisms on small spatial scales.

We thank the anonymous referee for insightful comments that helped us improve this paper. We thank Ed Moran as well as John Biretta and Tala Monroe of the STIS Instrument team for their help with some of the technical aspects of this work. This work was supported by funding from the Alfred P. Sloan Foundation's Minority Ph.D. (MPHD) Program, awarded to M. M. in 2014–15. This material is based upon work supported by the National Science Foundation Graduate Research Fellowship Program under Grant No. DGE1255832. Any opinions, findings, and conclusions or recommendations expressed in this material are those of the authors and do not necessarily reflect the views of the National Science Foundation. Support for program number *HST*-GO-12595.001-A was provided by NASA through a grant from the Space Telescope Science Institute, which is operated by the Association of Universities for Research in Astronomy, Inc., under NASA contract NAS5-26555. This work was performed in part at Aspen Center for Physics, which is supported by National Science Foundation grant PHY-1607611. L.C.H. was supported by the National Key R&D Program of China (2016YFA0400702) and the National Science Foundation of China (11473002, 11721303). This research has made use of the AstroBetter blog and Wiki, NASA's Astrophysics Data System, and the NASA/IPAC Extragalactic Database (NED), which is operated by the Jet Propulsion Laboratory, California Institute of Technology, under contract with the National Aeronautics and Space Administration. Research by A.J.B. is supported in part by NSF grant AST-1412693.

ORCID iDs

Mallory Molina https://orcid.org/0000-0001-8440-3613
Michael Eracleous https://orcid.org/0000-0002-3719-940X
Aaron J. Barth https://orcid.org/0000-0002-3026-0562
Jessie C. Runnoe https://orcid.org/0000-0001-8557-2822
Luis C. Ho https://orcid.org/0000-0001-6947-5846
Jonelle L. Walsh https://orcid.org/0000-0002-1881-5908

References

Allen, M. G., Groves, B. A., Dopita, M. A., Sutherland, R. S., & Kewley, L. J. 2008, ApJS, 178, 20
Baldwin, J. A., Phillips, M. M., & Terlevich, R. 1981, PASP, 93, 5
Barth, A. J., Filippenko, A. V., & Moran, E. C. 1999, ApJL, 515, L61
Barth, A. J., Reichert, G. A., Filippenko, A. V., et al. 1996, AJ, 112, 1829
Barth, A. J., & Shields, J. C. 2000, PASP, 112, 753
Belfiore, F., Maiolino, R., Maraston, C., et al. 2016, MNRAS, 461, 3111
Bertelli, G., Bressan, A., Chiosi, C., Fagotto, F., & Nasi, E. 1994, A&AS, 106, 275
Binette, L., Magris, C. G., Stasińska, G., & Bruzual, A. G. 1994, A&A, 292, 13
Binette, L., Wilson, A. S., & Storchi-Bergmann, T. 1996, A&A, 312, 365
Blandford, R. D., & Begelman, M. C. 1999, MNRAS, 303, L1
Boroson, T. A., & Green, R. F. 1992, ApJS, 80, 109
Bowers, C. D. 1997, in The 1997 HST Calibration Workshop, ed. S. Casertano (Baltimore, MD: Space Telescope Science Institute), http://www.stsci.edu/hst/stis/documents/calworkshop/1997
Brenneman, L. W., Weaver, K. A., Kadler, M., et al. 2009, ApJ, 698, 528
Bruzual, G., & Charlot, S. 2003, MNRAS, 344, 1000
Bujarrabal, V., Alcolea, J., Sahai, R., Zamorano, J., & Zijlstra, A. A. 1998, A&A, 331, 361
Capetti, A., Axon, D. J., & Macchetto, F. D. 1997, ApJ, 487, 560
Cappellari, M., & Emsellem, E. 2004, PASP, 116, 138
Cardelli, J. A., Clayton, G. C., & Mathis, J. S. 1989, ApJ, 345, 245
Cecil, G., Morse, J. A., & Veilleux, S. 1995, ApJ, 452, 613
Cid Fernandes, R., González Delgado, R. M., Schmitt, H., et al. 2004, ApJ, 605, 105
Claussen, M. J., Diamond, P. J., Braatz, J. A., Wilson, A. S., & Henkel, C. 1998, ApJL, 500, L129
Contini, M. 1997, A&A, 323, 71
Contini, M., & Viegas, S. M. 2001, ApJS, 132, 211
Dopita, M. A. 2002, RMxAA, 13, 177
Dopita, M. A., Fischera, J., Sutherland, R. S., et al. 2006, ApJS, 167, 177
Dopita, M. A., Groves, B. A., Sutherland, R. S., Binette, L., & Cecil, G. 2002, ApJ, 572, 753
Dopita, M. A., Ho, I.-T., Dressel, L. L., et al. 2015, ApJ, 801, 42
Dopita, M. A., Koratkar, A. P., Allen, M. G., et al. 1997, ApJ, 490, 202
Dopita, M. A., Koratkar, A. P., Evans, I. N., et al. 1996, in ASP Conf. Ser. 103, The Physics of Liners in View of Recent Observations, ed. M. Eracleous et al. (San Francisco, CA: ASP), 44
Dopita, M. A., & Sutherland, R. S. 1995, ApJ, 455, 468
Dudik, R. P., Satyapal, S., Gliozzi, M., & Sambruna, R. M. 2005, ApJ, 620, 113
Dudik, R. P., Satyapal, S., & Marcu, D. 2009, ApJ, 691, 1501
Eracleous, M., Hwang, J. A., & Flohic, H. M. L. G. 2010a, ApJ, 711, 796
Eracleous, M., Hwang, J. A., & Flohic, H. M. L. G. 2010b, ApJS, 187, 135
Eracleous, M., Shields, J. C., Chartas, G., & Moran, E. C. 2002, ApJ, 565, 108
Falcke, H., Nagar, N. M., Wilson, A. S., & Ulvestad, J. S. 2000, ApJ, 542, 197
Falcke, H., Wilson, A. S., & Simpson, C. 1998, ApJ, 502, 199
Falco, E. E., Kurtz, M. J., Geller, M. J., et al. 1999, PASP, 111, 438
Ferland, G. J., & Netzer, H. 1983, ApJ, 264, 105
Ferruit, P., Wilson, A. S., Whittle, M., et al. 1999, ApJ, 523, 147
Filho, M. E., Barthel, P. D., & Ho, L. C. 2002, A&A, 385, 425
Filho, M. E., Barthel, P. D., & Ho, L. C. 2006, A&A, 451, 71
Filippenko, A. V. 1996, in ASP Conf. Ser. 103, The Physics of Liners in View of Recent Observations, ed. M. Eracleous et al. (San Francisco, CA: ASP), 17
Filippenko, A. V., & Terlevich, R. 1992, ApJL, 397, L79
Flohic, H. M. L. G., Eracleous, M., Chartas, G., Shields, J. C., & Moran, E. C. 2006, ApJ, 647, 140
Fosbury, R. A. E., Mebold, U., Goss, W. M., & Dopita, M. A. 1978, MNRAS, 183, 549
Frank, A., & Mellema, G. 1994, A&A, 289, 937
Gabel, J. R., Bruhweiler, F. C., Crenshaw, D. M., Kraemer, S. B., & Miskey, C. L. 2000, ApJ, 532, 883
Girardi, L., Bressan, A., Bertelli, G., & Chiosi, C. 2000, A&AS, 141, 371
Giroletti, M., Taylor, G. B., & Giovannini, G. 2005, ApJ, 622, 178
González Delgado, R. M., Cid Fernandes, R., Pérez, E., et al. 2004, ApJ, 605, 127
Gonzalez Delgado, R. M., & Perez, E. 1996, MNRAS, 281, 1105
González Delgado, R. M., Pérez, E., Cid Fernandes, R., & Schmitt, H. 2008, AJ, 135, 747
González-Martín, O., Masegosa, J., Márquez, I., Guainazzi, M., & Jiménez-Bailón, E. 2009, A&A, 506, 1107

Graves, G. J., Faber, S. M., Schiavon, R. P., & Yan, R. 2007, ApJ, 671, 243
Groves, B. A., Dopita, M. A., & Sutherland, R. S. 2004, ApJS, 153, 9
Halpern, J. P., & Steiner, J. E. 1983, ApJL, 269, L37
Heckman, T. M. 1980, A&A, 87, 152
Helmboldt, J. F., Taylor, G. B., Tremblay, S., et al. 2007, ApJ, 658, 203
Ho, L. C. 2008, ARA&A, 46, 475
Ho, L. C., Filippenko, A. V., & Sargent, W. L. W. 1993, ApJ, 417, 63
Ho, L. C., Filippenko, A. V., & Sargent, W. L. W. 1997a, ApJS, 112, 315
Ho, L. C., Filippenko, A. V., & Sargent, W. L. W. 1997b, ApJ, 487, 568
Ho, L. C., Filippenko, A. V., & Sargent, W. L. W. 2003, ApJ, 583, 159
Jensen, J. B., Tonry, J. L., Barris, B. J., et al. 2003, ApJ, 583, 712
Jones, D. L., Wrobel, J. M., & Shaffer, D. B. 1984, ApJ, 276, 480
Kauffmann, G., Heckman, T. M., Tremonti, C., et al. 2003, MNRAS, 346, 1055
Kellermann, K. I., Vermeulen, R. C., Zensus, J. A., & Cohen, M. H. 1998, AJ, 115, 1295
Kewley, L. J., Dopita, M. A., Sutherland, R. S., Heisler, C. A., & Trevena, J. 2001, ApJ, 556, 121
Kewley, L. J., Groves, B., Kauffmann, G., & Heckman, T. 2006, MNRAS, 372, 961
Kriss, G. 1994, in ASP Conf. Ser. 61, Astronomical Data Analysis Software and Systems III, ed. D. R. Crabtree, R. J. Hanisch, & J. Barnes (San Francisco, CA: ASP), 437
Kurpiewski, A., & Jaroszyński, M. 1999, A&A, 346, 713
Laor, A. 1998, ApJL, 496, L71
Lauer, T. R., Ajhar, E. A., Byun, Y.-I., et al. 1995, AJ, 110, 2622
Luridiana, V., Morisset, C., & Shaw, R. A. 2015, A&A, 573, A42
Maoz, D. 2007, MNRAS, 377, 1696
Martins, L. P., Leitherer, C., Cid Fernandes, R., et al. 2004, in IAU Symp. 222, The Interplay Among Black Holes, Stars and ISM in Galactic Nuclei, ed. T. Storchi-Bergmann, L. C. Ho, & H. R. Schmitt (Cambridge: Cambridge Univ. Press), 337
Masegosa, J., Márquez, I., Ramirez, A., & González-Martín, O. 2011, A&A, 527, A23
Nagao, T., Murayama, T., Shioya, Y., & Taniguchi, Y. 2002, ApJ, 567, 73
Nagar, N. M., Falcke, H., & Wilson, A. S. 2005, A&A, 435, 521
Narayan, R., & Yi, I. 1995, ApJ, 452, 710
Nemmen, R. S., Storchi-Bergmann, T., & Eracleous, M. 2014, MNRAS, 438, 2804
Osterbrock, D. E. 1989, Astrophysics of Gaseous Nebulae and Active Galactic Nuclei (Mill Valley, CA: University Science Books)
Osterbrock, D. E., & Ferland, G. J. 2006, Astrophysics of Gaseous Nebulae and Active Galactic Nuclei (Sausalito, CA: University Science Books)
Papaderos, P., Gomes, J. M., Vílchez, J. M., et al. 2013, A&A, 555, L1
Phillips, M. M., Jenkins, C. R., Dopita, M. A., Sadler, E. M., & Binette, L. 1986, AJ, 91, 1062
Pogge, R. W., Maoz, D., Ho, L. C., & Eracleous, M. 2000, ApJ, 532, 323
Sabra, B. M., Shields, J. C., Ho, L. C., Barth, A. J., & Filippenko, A. V. 2003, ApJ, 584, 164
Sánchez-Blázquez, P., Peletier, R. F., Jiménez-Vicente, J., et al. 2006, MNRAS, 371, 703
Sarzi, M., Shields, J. C., Schawinski, K., et al. 2010, MNRAS, 402, 2187
Sevenster, M. N., & Chapman, J. M. 2001, ApJL, 546, L119
Shields, J. C. 1992, ApJL, 399, L27
Shull, J. M., & McKee, C. F. 1979, ApJ, 227, 131
Simões Lopes, R. D., Storchi-Bergmann, T., de Fátima Saraiva, M., & Martini, P. 2007, ApJ, 655, 718
Singh, R., van de Ven, G., Jahnke, K., et al. 2013, A&A, 558, A43
Sugai, H., Hattori, T., Kawai, A., et al. 2005, ApJ, 629, 131
Taniguchi, Y., Shioya, Y., & Murayama, T. 2000, AJ, 120, 1265
Terlevich, R., & Melnick, J. 1985, MNRAS, 213, 841
Tully, R. B. 1988, Nearby Galaxies Catalog (Cambridge: Cambridge Univ. Press)
Tully, R. B., Courtois, H. M., Dolphin, A. E., et al. 2013, AJ, 146, 86
Ulvestad, J. S., & Ho, L. C. 2001, ApJL, 562, L133
Van de Steene, G. C., & van Hoof, P. A. M. 2003, A&A, 406, 773
van Dokkum, P. G. 2001, PASP, 113, 1420
van Velzen, S., Falcke, H., Schellart, P., Nierstenhöfer, N., & Kampert, K.-H. 2012, A&A, 544, A18
Vanden Berk, D. E., Richards, G. T., Bauer, A., et al. 2001, AJ, 122, 549
Veilleux, S., & Osterbrock, D. E. 1987, ApJS, 63, 295
Vestergaard, M., & Wilkes, B. J. 2001, ApJS, 134, 1
Walsh, J. L., Barth, A. J., Ho, L. C., et al. 2008, AJ, 136, 1677
Wilson, A. S., & Raymond, J. C. 1999, ApJL, 513, L115
Wrobel, J. M. 1984, ApJ, 284, 531
Yan, R., & Blanton, M. R. 2012, ApJ, 747, 61
Yan, R., Newman, J. A., Faber, S. M., et al. 2006, ApJ, 648, 281